JFM PAPERS

Simultaneous impact of droplet pairs on solid surfaces

Anjan Goswami[1],[†] **and Yannis Hardalupas**[1],[†]

[1]Department of Mechanical Engineering, Imperial College London, London SW7 2AZ, UK

This study investigates the dynamics of the simultaneous impact of two droplets on a dry substrate. We develop a new micro-controlled droplet generator that releases two equally sized water droplets simultaneously on-demand, with no trailing droplets. The impact Weber number, based on impact droplet size and velocity, and the inter-droplet spacing relative to the impact droplet size are varied in the ranges of 54 to 155 and 1.32 to 2.25, respectively, leading to the strong interaction of the spreading lamellae that form a central uprising sheet, which eventually deposits or breaks into tiny droplets. We analyse the impact processes for both deposition and splashing of the uprising sheets. Simultaneous high-speed imaging from two orthogonal views of the droplet impacts quantifies the three-dimensional structure of the sheet morphology, including the temporal evolution of the rim-bounded 'semilunar' shape, surface waves, rim corrugations and finger formation, and deposition or splashing of the liquid sheet. The characteristics of the sheet surface waves and the rim instabilities are quantified. Novel scaling is developed for the maximum sheet height, sheet width and thickness, which considers the geometrical constraints and mass balance of the interacting lamellae to describe the temporal evolution of a 'semilunar' uprising sheet and is in good agreement with the measurements. The uprising sheet splashing generates larger droplets than those from splashing of single-droplet impacts, and it occurs due to the end-pinching of sheet fingers and at conditions that single-droplet impacts lead only to liquid deposition.

Key words: drops, breakup/coalescence, aerosols/atomization

1. Introduction

Droplet impact onto solid surfaces is ubiquitous in natural phenomena and practical applications. For instance, the impact of multiple droplets is common during rain in nature,

† Email addresses for correspondence: a.goswami19@imperial.ac.uk, y.hardalupas@imperial.ac.uk

during pesticide or nutrient spraying in agriculture, during drug delivery and medical treatments (nebulisers, cryogenic tissue cooling) and in industries (spray cooling, inkjet printing, surface coating, fuel injection). In particular, the outcome of the spray impact on surfaces depends on the impact behaviour of droplets and determines the deposited liquid mass and the generation of new liquid fragments, which move away from the surface.

The study of single-droplet impact on solid surfaces dates back to the pioneering experiment of Worthington (Worthington 1877). Many studies followed, which also considered time-resolved observations of the impact process over the last two decades using high-speed imaging (Thoroddsen, Etoh & Takehara 2008). The literature classifies droplet impact phenomena into two groups, namely single-droplet impact and multiple-droplet impact (Cossali, Marengo & Santini 2007; Cossali *et al.* 2007; Liang & Mudawar 2016; Yarin, Roisman & Tropea 2017; Breitenbach, Roisman & Tropea 2018; Ersoy & Eslamian 2020; Luo *et al.* 2021), depending on the concentration of impacting droplets and their interaction characteristics on the impact surface. A good understanding of the physics of single-droplet impact on both solid and liquid surfaces is available, see e.g. Josserand & Thoroddsen (2016), Marengo *et al.* (2011) and Yarin *et al.* (2006) for comprehensive reviews. The pertinent outcomes include splashing, deposition or bouncing of droplets and liquid spreading dynamics, and are mainly scaled by two dimensionless parameters: the Weber number $We = \rho V_0^2 D_0/\sigma$ and the Reynolds number $Re = \rho V_0 D_0/\mu$, where V_0 is the impact velocity, D_0 is the initial droplet diameter, and ρ, σ and μ represent the density, surface tension, and viscosity of the droplet liquid, respectively. The temporal evolution of single droplets after the impact is usually described using a non-dimensional time, defined as $\tau = tV_0/D_0$, where t is the dimensional time. A number of empirical correlations, based on *We* and *Re*, have been proposed for the deposition/splash boundary of single-droplet impacts on solid surfaces and the size of the liquid fragments generated after the splashing (Roisman, Lembach & Tropea 2015; Yarin *et al.* 2017; Burzynski, Roisman & Bansmer 2020).

However, multiple-droplet impacts on surfaces are more common in practical spraying processes and have not been investigated sufficiently (Liang & Mudawar 2016; Yarin *et al.* 2017; Fest-Santini *et al.* 2021). Figure 1 depicts multiple-droplet impact scenarios on a solid substrate with associated length and time scales labelled in figure 1(*a*). Depending on the spacing Δx between the centre of the droplets and their time difference Δt_i, the impacts of multiple droplets can be successive, simultaneous and non-simultaneous, as illustrated in figure 1(*b*). The non-simultaneous impact case is expected to be statistically much more frequent than the others. It is noted that when either Δx or Δt_i crosses a finite threshold level, a drop can deposit on a surface before the impact of a second drop, leading to a different phenomenology, i.e. one drop impacting next to a sessile drop (Gilet & Bourouiba 2015; Wang & Bourouiba 2018). Most multiple-droplet impact studies have investigated successive impacts through experiments (Barnes *et al.* 1999; Fujimoto, Ito & Takezaki 2002; Fujimoto, Tong & Takuda 2008; Deendarlianto *et al.* 2016; Zhang *et al.* 2017; Chen *et al.* 2020; Guggilla, Narayanaswamy & Pattamatta 2020; Wibowo *et al.* 2021) and numerical simulations (Fujimoto *et al.* 2001; Tong, Kasliwal & Fujimoto 2007; Raman *et al.* 2016; Zhang *et al.* 2017; Luo *et al.* 2021). These studies have considered the hydrodynamics for a range of impact conditions, including the time difference between impacts, liquid properties, surface wettability, surface roughness, surface curvature and surface inclination. It was also shown that the impact of multiple droplets on surfaces modifies the liquid fragments that are generated during splashing relative to those of single-droplet impacts (Barnes *et al.* 1999; Moreira, Moita & Panao 2010). The physical understanding of the simultaneous impact of multiple droplets onto
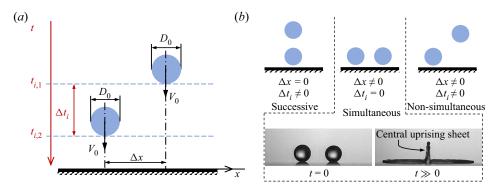
Figure 1. Multiple droplet impact on a solid surface. (*a*) Schematic of the associated length and time scales. (*b*) Schematic of successive, simultaneous and non-simultaneous impacts with respective criteria. Also, the touchdown condition (at $t = 0$) and the central uprising sheet (at $t \gg 0$) for a case of simultaneous impacts.

a solid surface and how multiple-droplet interactions affect the formation of new liquid fragments is still lacking. Partly, this omission is due to the difficulty of generating two droplets impacting simultaneously on a surface, as pointed out by several researchers (Tong *et al.* 2007; Liang *et al.* 2020). Such information can provide a physical understanding of the temporal evolution of droplet-pair impacts and potentially a reference for comparison to non-simultaneous impacts.

When two droplets simultaneously impact onto a solid surface, the spreading droplet lamellae interact and generate a central uprising sheet (figure 1). This central sheet may modify the splashing dynamics and the resulting liquid fragments. Barnes *et al.* (1999) showed that the central sheet can become unstable and generate droplets that are larger than those generated during single-droplet impacts. Roisman *et al.* (2002) developed a theoretical model for the temporal evolution of the central sheet height for simultaneous impacts of identical droplets, which has not been verified by experimental findings. An early study used two generators of continuous monodispersed droplet streams (Barnes *et al.* 1999), while recent studies used microchannel syringe pumps with needle vibrators (Liang *et al.* 2020; Gultekin *et al.* 2021) and a multichannel micropipette (Ersoy & Eslamian 2020) to deliver on-demand droplet pairs. However, these studies faced technical difficulties in reproducing simultaneous identical droplets. Therefore, they reported only one experimental observation of the vertical evolution of the sheet (i.e. like the bottom-right image of figure 1*b*) for a given Δx and *We* case, which they found as the best representative of a simultaneous impact case (Gultekin *et al.* 2021). However, the central sheet grows both vertically and laterally, and a simultaneous recording from different views is required to fully characterise the sheet evolution. The study of Ersoy & Eslamian (2020) recorded the central sheet evolution individually from two orthogonal views (namely front and side views), where the 'semilunar' shape of the uprising sheet became evident in the side-view images. However, the reported results were limited, and the instability and the breakup of the central sheet into liquid fragments were not studied.

For simultaneous droplet impacts on liquid films, the splashing of the central sheet is reasonably understood through experiments (Cossali *et al.* 2007) and numerical investigations (Liang *et al.* 2018; Fest-Santini *et al.* 2021). They recognised that the central sheet can disintegrate at a threshold level lower than that for equivalent single-droplet impacts in isolation (Cossali *et al.* 2007). However, for simultaneous droplet impacts onto dry solid surfaces, no detailed study of the splashing morphology is available, and the

characteristics of the central sheet and the resulting liquid fragments are largely unknown. In addition, the physical mechanism that determines the instability of the central sheet and its dependence on appropriate scaling parameters of droplet-pair impacts need to be determined.

The current study provides the first detailed morphological experimental characterisation of the temporal and spatial evolution of the central sheet and its splashing for simultaneous droplet-pair impacts on solid surfaces. It also develops a geometrical description of the underlying physics and provides a scaling model for the temporal evolution of the central sheet formed from the interacting individual lamellae. The rest of the paper is structured as follows. Section 2 describes the developed experimental approach for controlled ejection of simultaneous droplet pairs, the associated setup and the image processing approach. Section 3 reports the findings. It compares first a single-droplet impact to an equivalent droplet-pair impact with a particular focus on understanding the central sheet generation and the spreading dynamics of individual lamellae (§ 3.1). Then, the morphologies of the droplet impacts for different impact Weber numbers and inter-droplet spacings are discussed in § 3.2, followed by the geometrical description of the central sheet evolution (§ 3.3). Detailed quantitative analyses of the sheet evolution and spreading behaviour of the combined liquid mass are presented in § 3.4. The splashing characteristics of the central sheet are discussed in § 3.5. The paper ends with a summary of the main conclusions.

2. Experimental methodology

2.1. *Experimental arrangement*

The experiments use distilled water ($\rho = 996\,\mathrm{kg\,m^{-3}}$, $\sigma = 0.073\,\mathrm{N\,m^{-1}}$ and $\mu = 0.001\,\mathrm{mPa\,s}$), and the impact substrate is a smooth acrylic (synthetic polymer, PMMA) plate. The mean roughness of the impact surface (R_a) is 1.17 nm, measured using an optical microscope (Bruker-Nano, Contour GT-K). A drop shape analyser Kruss DSA 30 was used to measure the advancing θ_A and receding θ_R contact angles ($\theta_A = 80 \pm 2°$, $\theta_R = 58 \pm 2°$) of the water on the acrylic surface by a sessile drop method. Figure 2 shows a schematic representation of the experimental setup. An in-house-built syringe pump was used to deliver the distilled water to the needle assembly. During each experiment, two equal-sized water droplets were simultaneously released from the blunt needle tips and allowed to impact the acrylic substrate. The impact process was recorded by a high-speed image acquisition unit, and the experimental data were extracted by post-processing the recorded images. A three-dimensional Cartesian coordinate system is defined for the impact process, as shown in figure 2. The origin of this coordinate system lies on the impact surface, in the middle of the impacting droplets. The initial droplet diameter (D_0) was kept constant at 3.13 ± 0.04 mm and the impact Weber number (*We*) was varied by adjusting the droplet release height.

Two monochromatic high-speed cameras were synchronised to record simultaneously the front (Photron, FASTCAM APX RS) and side (Photron, FASTCAM SA1.1) perspectives of all impact processes. Both cameras were operated with a recording rate of 9000 frames/s and an exposure time of 5 µs. A standard micro-ruler, with a precision of 0.01 mm, was used to calibrate the window view of each camera. The effective spatial resolutions of the front and side cameras were 0.03 and 0.04 mm per pixel, respectively. The impact area was illuminated uniformly by two diffuser-paired LED lamps, arranged in a traditional shadowgraph imaging configuration (see figure 2).
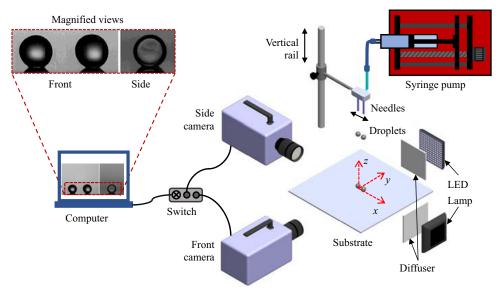
961 A17-4

Figure 2. Schematic representation of the experimental arrangement (not to scale). The origin of the coordinate system is set on the substrate, in the middle of impacting droplets.

2.1.1. *Droplet generator*

A droplet generator was developed which had the ability to ensure simultaneous delivery of two same-size droplets. The droplet generator consists of two major parts: a customised needle assembly and an in-house-built 3-D printed syringe pump. The needle assembly includes two blunt tip removable needles with a mechanism to adjust the spacing between the needles, i.e. to precisely control the inter-droplet spacing (Δx) during experiments. The programmable syringe pump has a microcontroller (Arduino Uno) and motor shield-based control system to actuate a fine stepper motor of the pump to precisely deliver liquid water through the needles (figure 2). The droplet generator was programmed to operate in three modes on demand: (i) droplet ejection; (ii) liquid jetting; and (iii) refilling. For the case of droplet ejection mode, the set speed and steps of the pump motor allow a certain amount of liquid to dispense out to each needle, leading to simultaneous single-droplet ejections with minimum oscillation. Any trapped air at the needle tips can lead to a non-simultaneous ejection of droplets. The liquid jetting operation mode allows draining out a volume of liquid to ensure air-free needle tips. Therefore, before ejecting the test droplets, a visible liquid meniscus was achieved at each needle tip through the liquid jetting operation. The syringe reservoir of the droplet generator can be refilled by a suction process, actuated by a reverse rotation of the pump motor.

2.2. *Image post-processing*

Several image processing routines were implemented in MATLAB to analyse the grey-scale images in batches (pre-impact or post-impact) to quantify the characteristics of the impact process. First, the quality of all images of a dataset was enhanced by applying the same filtering operations. Then, for a predefined batch of sequential images, an image processing routine binarised each image using a threshold value computed independently by applying Otsu's method (Otsu 1979) to each image. It is noted that changing the computed Otsu's threshold by $\pm 10\,\%$ led to negligible changes in the measured values.

Finally, the binary images were processed further to obtain the measured quantities. The uncertainty in the pixel measurement was ± 1 pixel, equivalent to 0.03 mm and 0.04 mm in the front-view and side-view images, respectively. The frame of the droplets' touchdown on the surface was considered as the time reference frame with time $t = 0$. The initial parameters, i.e. D_0, Δx and V_0, were measured from a predefined batch of consecutive images before impact. The D_0 was calculated from $D_0 = \sqrt{4A_d/\pi}$, where A_D represents the projected area of the droplet in an image. The V_0 was calculated from the displacement of the droplets between two successive images. The uncertainty of the velocity estimation was within $0.025 \, \text{m s}^{-1}$. The characteristics of the central sheet evolution and the liquid spreading on the impact surface were also extracted from image processing routines and will be presented in related sections.

It is noted that even though the two droplets were released nominally simultaneously following the procedure of § 2.1.1, they sometimes arrived at the impact surface with one or two frame delays. This delay happened due to slight differences in each droplet distortion during release. However, in this study, we consider only droplet impacts that occur at the same frame, representing a timescale of ≈ 0.11 ms (for the selected 9000 fps). In addition, for all these simultaneous droplet impact cases, we maintained a sample size of $N \geq 3$ per experimental case and the reported data represent the average value of the replicate events. It is noted that the vertical liquid sheet could not always be exactly captured from the side (i.e. front view). An angle between the y-axis (figure 2) and the camera axis was observed for some cases, as reflected by the sheet's projection in the front-view images (see figures 4 and 7). Apart from any inevitable misalignment in the optical arrangement, this angle could also be attributed to small differences in the diameter (or sphericity) of the two droplets, which influence the early stage of their interaction. For the dataset of the present study, the maximum angle between the central sheet axis and the camera axis is approximately $3°$.

3. Results and discussion

In this section, starting with the central sheet formation mechanism, we will discuss the effect of the impact Weber number and inter-droplet spacing on the central sheet evolution, spreading and splashing dynamics, with a particular focus on characterising the outcomes of the impact processes.

3.1. *Impact of two droplets: lamella spreading dynamics and central sheet formation*

This section provides a comparison between the dynamics of two-droplet impacts (with dimensionless inter-droplet spacing $\Delta x^* = \Delta x/D_0 = 1.80$) and an equivalent single-droplet impact case ($We \approx 80$, $Re \approx 3750$, $D_0 = 3.12 \pm 0.02$). This allows establishing, initially qualitatively, the way that the dynamics change during the simultaneous two droplet impacts. The single-droplet impact was accomplished by masking one of the needles of the droplet-pair generator to allow the delivery of a single droplet. Figure 3(a) presents a selection of front-view images at different dimensionless times ($\tau \approx 0 - 20$) of the impact of the single droplet and the droplet pair (see also supplementary movie 1 available at https://doi.org/10.1017/jfm.2023.249). Upon impact, the liquid lamella that emerges underneath each droplet starts to spread radially outwards on the surface, with a continuous decrease in the impacting droplet height. The spreading of the lamella on the surface is characterised by an instantaneous spread radius, $R(t)$, which is defined in figure 3(b) for both impact processes.
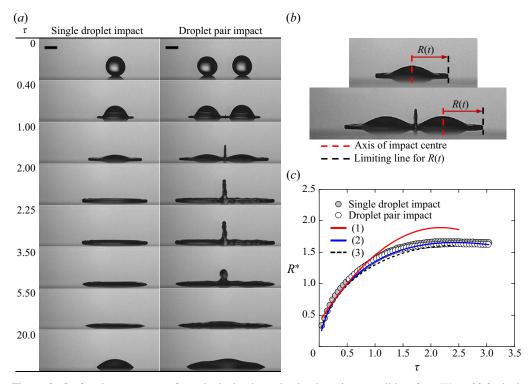
Figure 3. Surface impact process for a single droplet and a droplet pair on a solid surface ($We = 80$ for both cases, and $\Delta x^* = 1.80$ for the droplet pair). (*a*) Front-view images of the temporal evolution of the impact processes. Scale bars are 2 mm. (*b*) Schematic of the calculation of spread radius ($R(t)$) from the impact centre of a droplet for both cases. (*c*) Dimensionless spread radius ($R^* = R/D_0$) as a function of dimensionless time ($\tau = tV_0/D_0$) for both cases, in comparison to the theory of (1) Roisman *et al.* (2002), (2) Gordillo, Riboux & Quintero (2019) and (3) the empirical model by Lejeune, Gilet & Bourouiba (2018). See supplementary movie 1 for the corresponding video.

For the single-droplet impact with $We \approx 80$ (figure 3*a*), the rim-bounded spreading lamella reaches a maximum spread radius (R_{max}) at $\tau \approx 2.25$. At R_{max}, the contact line remains stationary while a receding contact angle is achieved at the lamella periphery, and subsequently, the liquid contact retracts back towards the impact centre. This receding liquid eventually deposits on the surface with an equilibrium shape at $\tau > 20$ (see supplementary movie 1). However, for the droplet-pair impact with $\Delta x^* = 1.80$ and $We \approx 80$ (figure 3*a*), the individual spreading lamellae start interacting with each other at the initial stage of their spreading ($\tau \approx 0.4$). Due to the high kinetic energy of the lamellae, their interaction generates an uprising liquid sheet along the line of intersection. During this stage, stagnation points form on the surface at the intersection line, and the interacting liquid flows are redirected laterally and vertically on the impact surface (Batzdorf *et al.* 2017; Gultekin *et al.* 2021). The central uprising sheet grows rapidly, reaches a summit ($\tau \approx 2.25$), and falls back on the liquid mass underneath due to surface tension and gravity ($\tau \approx 5.5$). The surface liquid also recedes, similar to the single-droplet case, and finally attains an equilibrium shape after $\tau \approx 20$. For the single- and droplet-pair cases, the final equilibrium shape resembles a single sessile drop (see supplementary movie 1). The images of figure 3(*a*) indicate that the spreading of the non-interacting lamella segments remains unaffected on the impact surface during the formation and growth of the central

uprising sheet. Roisman *et al.* (2002) also demonstrated similar spreading behaviour using the top-view images of droplet-pair impacts.

For the isolated and non-isolated impact cases of figure 3(*a*), we applied an image analysis algorithm that determines the impact centre of a droplet and measures the instantaneous spread radius ($R(t)$), as defined in figure 3(*b*). The temporal evolution of the dimensionless spread radius ($R^*(\tau) = R(t)/D_0$) for single-droplet and droplet-pair impacts up to $\tau \approx 3.0$ is shown in figure 3(*c*). For the isolated single droplet, R^* of the advancing lamella reaches a maximum value, which is approximately 1.65 times the initial droplet diameter (D_0) at $\tau \approx 2.25$ and then R^* decreases as the lamella recedes. For the non-isolated droplets of the droplet pair, R^* was measured from $\tau = \tau_0 \approx 0.4$, where τ_0 is the instant of the initiation of lamella interaction. The temporal evolution of R^* of the non-isolated droplets superposes on that of the isolated single droplet, with a negligible relative difference (maximum of 1.7 %), see figure 3(*c*). This superposition corroborates the idea that, for the droplet-pair impact, the portion of the liquid lamella that does not contribute to the central sheet formation spreads on the dry substrate, remaining unaffected by the ascending central sheet.

Numerous theoretical relations exist to estimate the maximum spread radius (R_{max}) on dry solid substrates in terms of different dimensionless parameters, which are individually a function of the impact parameters (Josserand & Thoroddsen 2016). However, such theoretical relations for the time-dependent spread radius, $R(t)$, are far less reported in the literature (Yarin *et al.* 2006). An earlier study of Roisman *et al.* (2002) considered the mass and momentum balance equations of a lamella rim to develop an analytical model, which allows estimating $R(t)$ in a dimensionless form as

$$R^*(\tau) = A(\tau + \omega) - B(\tau + \omega)^2, \tag{3.1}$$

where A, B and ω are three dimensionless parameters which depend on the Weber number *We*, the Reynolds number *Re* and the static advancing contact angle θ_A (see Roisman *et al.* (2002) for related details). It is noted that (3.1) was developed for $1 \leq \tau \leq \tau_{max}$, where τ_{max} is the dimensionless time that corresponds to the dimensionless maximum spread radius (R^*_{max}). Using the experimental parameters of the impact processes of figure 3(*a*), we obtain $A \approx 1.48$, $B \approx 0.32$ and $\omega \approx 0.27$. The prediction of (3.1) is compared to the current measurements in figure 3(*c*), where the theoretical line is extended for $\tau < 1$ and slightly for $\tau > \tau_{max}$. Although (3.1) predicts the time for R^*_{max} approximately in agreement with that for the measured R^*_{max} (i.e. $\tau_{max} \approx 2.25$), it overestimates R^*_{max} with a relative mean error of ≈ 11.84 %. Other authors also find similar divergence, e.g. a relative mean error of 11.64 ± 5.94 % (Ukiwe & Kwok 2005) and 14.17 ± 1.88 % (Ukiwe, Mansouri & Kwok 2005), while comparing their measured R^*_{max} to the prediction of (3.1). The limitation of this theoretical model lies primarily in the fact that the authors approximated the droplet shape as a circular disc of constant thickness from $\tau = 1$, which is 'not correct' as mentioned in a later study (Roisman, Berberović & Tropea 2009). Figure 3(*a*) also reveals, for both single and droplet pair cases, that the disk shape is not flat at $\tau = 1$, but becomes flat at $\tau \approx 2$. In addition, the contact line velocity of the spreading lamella is equated to the impact velocity (V_0) in this theory, whereas the contact line velocity of a spreading lamella is several times larger than the droplet impact velocity (Ukiwe & Kwok 2005). The temporal evolution of the velocity of the lamella contact lines and that of the central uprising sheet is detailed in Appendix A. Considering more realistic hypotheses and by applying mass and momentum balances at the lamella rim, Gordillo *et al.* (2019) deduced a set of ordinary differential equations that govern the time-dependent spread radius $R^*(\tau)$. We numerically solved their equations using MATLAB for our experimental conditions, and figure 3(*c*) also presents the obtained
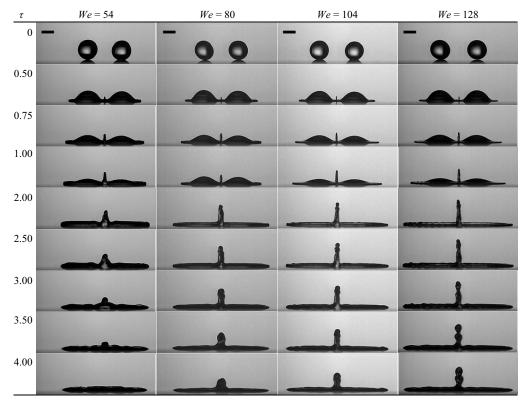
Figure 4. Central sheet evolution at different impact Weber numbers (front view: x–z plane of figure 1). The inter-droplet spacing is kept constant at 5.65 ± 0.15 mm ($\Delta x^* = 1.80 \pm 0.03$). Here, τ is the dimensionless time. Scale bars are 2 mm. See supplementary movies 2–5 for the corresponding videos.

droplet spreading radius $R^*(\tau)$ (for a hydrophilic surface and in our dimensionless form), which is in excellent agreement with our measurements. Recently, Gorin *et al.* (2022) also observed similar agreement with the theory of Gordillo *et al.* (2019) for both Newtonian and non-Newtonian droplet impacts. Figure 3(c) also presents $R^*(\tau)$ from the empirical model of Lejeune *et al.* (2018) and shows a reasonably good agreement with our measurements.

3.2. *Morphology of the central sheet evolution*

3.2.1. *Effect of impact Weber number*

Figures 4 and 5 respectively show a series of front-view and side-view images of the simultaneous impacts of two droplets at different dimensionless times for four different impact Weber numbers (*We*) with a fixed inter-droplet spacing of $\Delta x^* = 1.80 \pm 0.03$ (see also supplementary movies 2–5). These images reveal the morphology of the central sheet evolution in vertical and lateral directions. For all cases, the kinetic energy of the droplets is high enough to generate a central sheet, with its height increasing up to a certain time and then decreasing gradually, remaining vertical on the substrate. The dimensionless time for the onset of the lamella interaction (τ_0) does not vary significantly with the impact *We*, i.e. τ_0 is approximately 0.4 for all four cases. The relatively small inter-droplet spacing allows the two lamellae to interact during their initial spreading phase ($\tau < 1$). It is evident in figure 4 that a lamella becomes thinner with an increasing *We*, yielding a relatively thinner
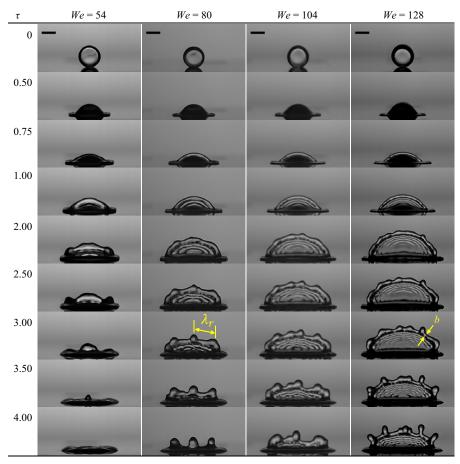
Figure 5. Central sheet evolution at different impact Weber numbers (side view: y–z plane of figure 1). The inter-droplet spacing is kept constant at 5.65 ± 0.15 mm ($\Delta x^* = 1.80 \pm 0.03$). Here, τ is the dimensionless time. Scale bars are 2 mm. Additionally, λ_r and b (shown at $\tau = 3$) are the instantaneous wavelength of the rim instability and the instantaneous rim thickness, respectively. See supplementary movies 2–5 for the corresponding videos.

central sheet at a higher *We*. The onset of central sheet formation does not appear in the images of figure 5 due to the height of the descending droplets. The ascending sheets become evident as their sizes exceed the descending droplet views at $\tau \approx 0.75$. In all cases, the ascending central sheet is bounded by a rim owing to surface tension effects, and the rim grows at the expense of the liquid sheet. The images at $\tau = 1$ (figure 5) show that the thickness of the outer rim decreases with increasing *We* due to the higher liquid kinetic energy relative to surface tension. All the rim-bounded ascending central sheets grow with a 'semilunar' shape, resulting from the action of lamella velocity components at the base of the sheet.

Figure 6(*a*) shows simplified schematics for two identical interacting lamellae on a smooth impact substrate. The interaction of these lamellae starts with their contact line points having $\alpha = 0$ (at the origin of the coordinate system), with the time-dependent lamella velocity V_L for $\tau = \tau_0$ (figure 6*a*-i). Subsequently, the continued lamella spreading leads to increasing interacting contact points along the y-axis and symmetrically about the x-axis, forming the linear sheet base for $\tau > \tau_0$ (figure 6*a*-ii). It is noted that the lamella velocity decreases with time, and therefore, a later interaction point (having $\alpha > 0$)
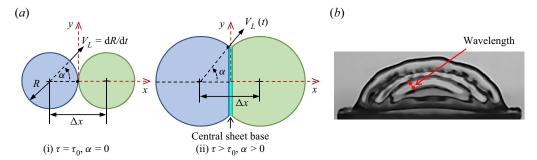
961 A17-10

Figure 6. (*a*) Schematic of the interaction of identical spreading lamellae: (i) at their first instant of interaction ($\tau = \tau_0$); and (ii) at $\tau > \tau_0$. Here, V_L is the lamella velocity that decreases as the spread radius R increases with time, α is the angle for any interaction point on the linear sheet base and $\alpha = 0$ corresponds to the first interaction point of the sheet base. (*b*) Concentric waves on the central sheet surface with the wavelength shown by red arrows.

initiates with a lower V_L than for $\tau = \tau_0$, and this V_L has two components, $V_L \cos \alpha$ and $V_L \sin \alpha$, respectively, along the *x*- and *y*-axes. The *x*-velocity component $V_L \cos \alpha$ that decreases with increasing α dictates the vertical growth of the central sheet, whereas the *y*-velocity component $V_L \sin \alpha$ that increases with α dictates the lateral extension of the sheet. Therefore, in the case of an ascending central sheet, usually, the velocity of the uprising liquid is maximum in the middle of the sheet and minimum at both ends of the sheet base, yielding the 'semilunar' shape of the central sheets of figure 5.

Figure 5 shows that concentric waves propagate towards the ascending 'semilunar' central sheet rim, similar to the capillary waves that occur during droplet impact onto thin liquid films (Yarin & Weiss 1995). These wavelengths (shown in figure 6*b*) were measured with ImageJ software and found to reduce from 0.52 ± 0.02 mm to 0.41 ± 0.01 mm and 0.26 ± 0.01 mm for increasing *We* of 80, 104 and 128, respectively. The mechanisms that may contribute to the instabilities across the central sheet are considered below.

The central sheet ascends vertically in ambient quiescent air due to the interaction of two expanding lamellae. If we model the first interaction of these two lamellae as an impact of one liquid lamella with a stationary object (in this case, the second lamella), the inertia at impact for the considered model would be twice the average inertia of the expanding lamellae. Accordingly, a lamella impact Weber number can be considered as $We_{L,imp} = 2\rho V_{0,imp}^2 T_L / \sigma$, where $V_{L,imp}$ is the average velocity of the interacting lamella edges and T_L is the average thickness of the lamella edges at $\tau = \tau_0$. For $We = 128$ and $\Delta x^* = 1.80$ (highest *We* of figure 5), we measured $V_{L,imp} \approx 2.8$ m s^{-1}, $T_L \approx 0.22$ mm from images, resulting in $We_{L,imp} \approx 47$, which is two orders of magnitude smaller than the critical Weber number of the flapping instability for a horizontally expanding sheet in air (i.e. $We_{cr} \simeq 10^3$ Bremond, Clanet & Villermaux 2007; Villermaux & Clanet 2002). Therefore, the capillary waves of the central sheets are expected to propagate towards the sheet rim without amplification, leading to no flapping instability (i.e. left and right movement) at the central sheet edge. The temporal and spatial evolution of the uprising central sheets of figure 5 supports the 'no-flap' condition since no sign of flapping is observed. In addition, the measured central sheet wavelengths remain sub-millimetre and much smaller than the capillary wavelength limit for a water–air interface, i.e. less than 1.725 cm as quantified from the analysis of Liu, Kijanka & Urban (2020).

The propagating waves along the central sheet eventually thicken the uprising sheet rim. At some instant, the rim becomes unstable due to contributions from gravity and surface tension and corrugated for relatively high *We*, i.e. images for $We = 80$, 104 and

We	N_C	λ_r (mm)	b (mm)	$\lambda_{RP} = 4.5b$ (mm)
80 ± 2	3	2.94 ± 0.18	0.63 ± 0.06	2.84 ± 0.27
104 ± 1	4	2.10 ± 0.22	0.51 ± 0.04	2.30 ± 0.16
128 ± 2	6	1.95 ± 0.16	0.45 ± 0.04	2.03 ± 0.18

Table 1. Comparison of the measured sheet rim instability wavelength (λ_r) with the wavelength of the fastest growing mode of Rayleigh–Plateau instability (λ_{RP}) at $\tau \approx 3.0$ for different impact Weber numbers (We). Here, N_C and b are the measured number of corrugations and the average rim thickness at $\tau \approx 3.0$, respectively.

128 at $\tau \approx 2.5$ of figure 5. The destabilisation and corrugations of a rim have been attributed to Rayleigh–Taylor (RT) instability (Taylor 1950; Villermaux & Bossa 2011; Peters, van der Meer & Gordillo 2013), Rayleigh–Plateau (RP) instability (Rayleigh 1878; Rozhkov, Prunet-Foch & Vignes-Adler 2002; Zhang *et al.* 2010), and a combination of Rayleigh–Taylor and Rayleigh–Plateau (coupled RT-RP) instabilities (Agbaglah, Josserand & Zaleski 2013; Agbaglah & Deegan 2014; Krechetnikov 2010; Roisman 2010; Wang *et al.* 2018; Wang & Bourouiba 2021). Therefore, uncertainties remain on the relevant underlying physics. In addition, the instability mechanism specifically for a central sheet rim has not been evaluated yet. In the present study, an uprising liquid rim (high-density fluid) decelerates in air (low-density fluid). The onset of the uprising rim destabilisation and the consequent initial corrugations (up to $\tau \approx 2.5$ in figure 5) can be attributed to the RT mechanism (Taylor 1950). After $\tau \approx 2.5$, the central sheets start to retract, and the rim corrugations become more pronounced and distinguishable (see images for $We = 80$, 104 and 128 in figure 5). The distribution of the corrugations appears to be almost symmetric around the z-axis of the coordinate system, and the number of corrugations (N_C) increases for higher We (see images at $\tau = 3.0$ of figure 5).

Recent studies (Agbaglah *et al.* 2013; Wang *et al.* 2018; Wang & Bourouiba 2021) considered the coupled RT-RP instability for the sheet rim instability evolution and concluded that the RP is the dominant mechanism at later times. The average distance of the rim corrugations is close to the wavelength of the fastest-growing mode of the RP instability (Rayleigh 1878), which is $\lambda_{RP}(\tau) = 4.5b(\tau)$, where b (defined in figure 5 and the measured values reported in table 1) is the average rim thickness. For $\tau \approx 3.0$, table 1 shows the measured average wavelength of the rim instability λ_r (defined in figure 5) for $We = 80$, 104 and 128, and λ_r is close to the corresponding λ_{RP}. Therefore, the rim of the central sheet is destabilised by the combined Rayleigh–Taylor and Rayleigh–Plateau mechanisms, in agreement with the findings of Krechetnikov (2010), Roisman (2010), Agbaglah *et al.* (2013), Agbaglah & Deegan (2014), Wang *et al.* (2018) and Wang & Bourouiba (2021) for different geometries. At later times, adjacent corrugations merge at some locations (see figure 5 for $We = 104$ and 128). At $\tau \approx 4$, the corrugations result in protruding finger-like structures due to the increased amplitude of the rim instability for higher We (i.e. $We = 80$, 104 and 128). For $We > 128$, protruding fingers appear on the ascending central sheet, which can disintegrate into secondary droplets. The splashing of the central sheet will be further discussed in § 3.5.

3.2.2. *Effect of inter-droplet spacing*

Figures 7 and 8 respectively show the front-view and side-view images of the simultaneous impacts of two droplets for four different inter-droplet spacings (Δx^*) with a fixed impact Weber number $We = 62 \pm 1$ (see also the supplementary movies 6–9). The instant of the start of the lamella interaction (τ_0) increases with the increase of inter-droplet spacing, e.g.
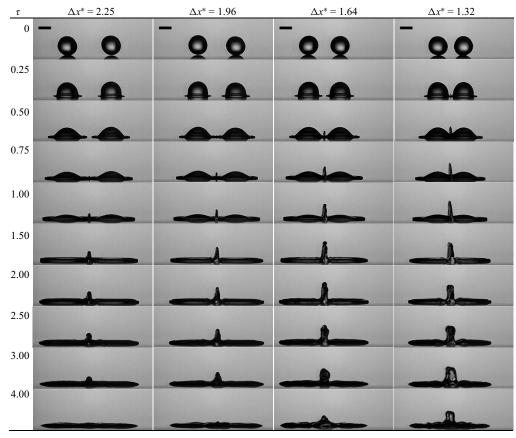
Figure 7. Central sheet evolution for different inter-droplet spacings (front view: x–z plane of figure 1). Here, $\Delta x^*(= \Delta x/D_0)$ is the inter-droplet spacing with respect to the initial droplet diameter, and τ is the dimensionless time. Scale bars are 2 mm. The Weber number is fixed at $We = 62 \pm 1$. See supplementary movies 6–9 for the corresponding videos.

$\tau_0 \approx 0.25$ for $\Delta x^* = 1.32$ and $\tau_0 \approx 0.75$ for $\Delta x^* = 2.25$. For larger Δx^*, the spreading lamellae lose more kinetic energy through viscous dissipation due to the prolonged spreading before the interaction. Consequently, the interaction of the lamellae reduces with increasing Δx^*, yielding a less pronounced central uprising sheet at larger Δx^* (figures 7 and 8).

For $\Delta x^* = 2.25$, 1.96 and 1.64, figures 7 and 8 show that the vertical evolution and the 'semilunar' shape of the central sheet appear at different times, but have similar characteristics to observations in figures 4 and 5 for different Weber numbers. For $\Delta x^* = 1.32$ though, the droplet interaction and the central sheet evolution are somehow different from the other cases in two ways.

(a) The vertically descending bulk liquid portions of the two droplets come in contact and start contributing to the central sheet evolution due to the closeness of the impacting droplets for $\Delta x^* = 1.32$. For the other three cases, the sheet evolves only through the interaction of the thin lamella portions (see images at $\tau \approx 0.5$ in figure 7). Gordillo *et al.* (2019) theoretically defined two 'spatio-temporal' regions of a single spreading droplet, namely the 'drop-region' and the 'lamella-region'.
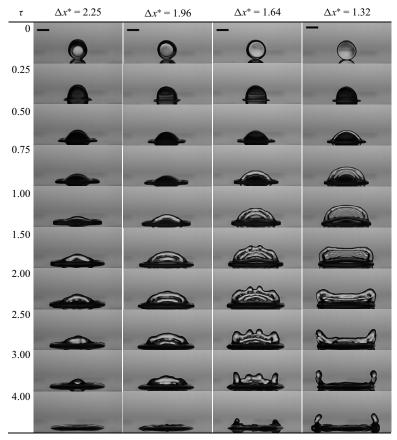
Figure 8. Central sheet evolution for different inter-droplet spacing (side view: y–z plane of figure 1). Here, $\Delta x^*(=\Delta x/D_0)$ is the dimensionless inter-droplet spacing, and τ is the dimensionless time. Scale bars are 2 mm. The Weber number is fixed at $We = 62 \pm 1$. See supplementary movies 6–9 for the corresponding videos.

They divided the instantaneous dimensionless spread radius $R^*(\tau)$ (defined in figure 3) into two parts as $R^*(\tau) = r^*_{d-r}(\tau) + r^*_{l-r}(\tau)$, where $r^*_{d-r}(\tau)$ defines the instantaneous 'drop-region' for $0 \le r^*_{d-r}(\tau) \le \sqrt{3\tau/2}$, and $r^*_{l-r}(\tau)$ defines the instantaneous 'lamella-region' for $\sqrt{3\tau/2} \le r^*_{l-r} \le R^*(\tau)$. Therefore, for droplet-pair impacts, at any instant τ, the two drop regions interact with each other if the spatio-temporal separator $\sqrt{3\tau/2}$ exceeds half of the inter-droplet spacing, i.e. if $\sqrt{3\tau/2} > \Delta x^*/2$. Note that Gordillo *et al.* (2019) used impacting droplet radius ($R_0 = D_0/2$) as the length scale for their dimensionless time, whereas we use D_0 for τ. For $\Delta x^* = 1.32$ and $\tau = 0.5$, we find $\sqrt{3\tau/2} \approx 0.87$, which considerably exceeds $\Delta x^*/2 \, (= 0.66)$, indicating that the interaction of the two drop regions occurs at $\tau < 0.5$, i.e. at the early stage of the phenomenon (figure 7 for $\Delta x^* = 1.32$). The descending bulk liquid of the drop region not only has a radial velocity like a spreading lamella but also has a downwards velocity as the liquid is yet to collapse on the impact surface.

(b) For $\Delta x^* = 1.32$, the central sheet appears to descend suddenly at $\tau \approx 1.5$, whilst all other three central sheets are still ascending (figures 7 and 8). The 'semilunar'

central sheet becomes evident at $\tau \approx 0.5$, earlier than for all other cases. However, the growth of the ascending central sheet appears to be more dominant in the lateral direction compared to the upwards direction, as suggested by the flat-topped central sheet at $\tau \approx 1$ (figure 8 for $\Delta x^* = 1.32$). This means that, at the intersection line, the redirection of the interacting liquid flows is more prominent towards the sides compared to the upwards direction. This preferential lateral growth of the sheet can be attributed to the direct interaction of vertically descending with considerable velocity bulk droplet liquid. The dominant lateral liquid flow in the sheet leads to significant stretching of the rim that causes minimum thickness on the central axis (see image at $\tau \approx 1.5$ in figure 8). In addition, at $\tau \gtrsim 1.5$, the sheet starts descending symmetrically around its central axis due to gravity, forming two prominent cusps at the sides that look like 'hornlike' structures after the inner portion of the sheet falls back on the surface. The inclined shape of these 'horns' facilitates their appreciably slower descent and thus retains the existence of the central sheet for a relatively long time. This unique central sheet evolution for small inter-droplet spacings is identified for the first time and can influence the liquid fragments generated during splashing. Consequently, additional physical processes must be considered to predict the liquid sheet instabilities for small values of Δx^*.

3.3. *Geometrical description of the central sheet growth*

The morphology and temporal evolution of the central sheet, shown in § 3.2, demonstrate that the vertical central sheet forms and grows at the expense of the horizontal spreading lamellae. The expense of the horizontal lamellae can be reflected on the x–y plane by two truncated circles combined at the central sheet base, as shown in figure 6(*a*). For all cases, the side views of the central sheet resemble a circular segment on the y–z plane up to a certain time of the sheet evolution (see figures 5 and 8 and supplementary movies 2–9). A custom-made image analysis algorithm was used to fit a circle to the outer rim boundary of the central sheet and evaluate its centre and circle radius, which represents the radius of curvature (R_S) of the central sheet. Figure 9 shows the processed images with the superimposed circle at different dimensionless times for impacts with $We = 128$ and $\Delta x^* = 1.80$. The imaging software also quantifies the width of the central sheet (W_S) on the impact surface from the intersection points (blue square markers in figure 9) of each circle and the corresponding solid surface line. However, at the late stages of the impact process, e.g. at $\tau > 1.75$ for the impact conditions of figure 9, the central sheet loses its stability, and its unstable outer rim does not fit well to the circular shape. The evolution of the radius of curvature and the width of the sheet will be reported in § 3.4. However, the observations of figure 9 can be used to describe the temporal evolution of the vertically ascending central sheet from the temporal expense of the horizontally spreading lamellae.

Figure 10 shows the schematic diagrams for a geometrical description of a vertically ascending central sheet. For simultaneous impacts of two identical droplet sizes moving with the same velocity, the initial diameter of the left and right droplets (i.e. $D_{0,L}$ and $D_{0,R}$) and their impact velocities (i.e. $V_{0,L}$ and $V_{0,R}$) can be equated to $D_{0,L} = D_{0,R} = D_0$ and $V_{0,L} = V_{0,R} = V_0$, respectively. Upon impact on an isotropic flat surface, the lamellae of these droplets spread with identical circular contact lines with an instantaneous radius $R(t)$ (figure 10*a*) and touch each other in the middle of a fixed inter-droplet spacing $\Delta x > D_0$. As these lamellae evolve in time, a segment from both left and right lamellae with an equal instantaneous area of $A_{LS1}(t)$, as illustrated in figure 10(*a*), contributes to the formation and growth of a central uprising sheet. Therefore, the area of the lamella segment A_{LS}, which
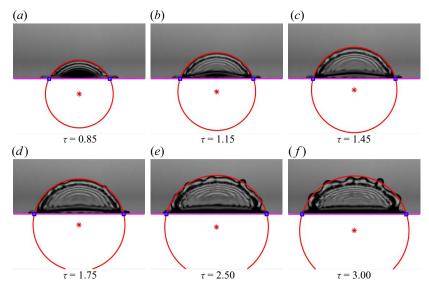
Figure 9. Determination of the radius of curvature of the central sheet (R_S) from its side view (on the y–z plane of figure 1) images through best-fit circles at the outer rim boundary of the sheets. The width of the central sheet (W_S) is determined from the intersection points (blue square markers) of the horizontal magenta line (impact surface) and the fitted red circle. The images correspond to droplet-pair impacts with $We = 128$ and $\Delta x^* = 1.80$. For convenience, the pixels underneath the surface line are converted into white pixels.

contributes to the central sheet at a time t, can be expressed in a dimensionless form as

$$A_{LS}^*(\tau) \approx 2A_{LS1}^*(\tau) = R^{*2}(\tau) \left\{ 2\arccos\left(\frac{\Delta x^*}{2R^*(\tau)}\right) - \sin\left[2\arccos\left(\frac{\Delta x^*}{2R^*(\tau)}\right)\right]\right\}. \tag{3.2}$$

Figure 10(b) shows the schematic of the growth of the 'semilunar' uprising sheet with its instantaneous area $A_S(t)$, radius of curvature $R_S(t)$ and width on the impact surface $W_S(t)$. These quantities can be measured from the images, as demonstrated in figure 9. For convenience, the 'width of the sheet on the impact surface' will be termed as 'sheet width' in the forthcoming discussions. The dimensionless instantaneous central sheet area $A_S^*(\tau)$ can be expressed as

$$A_S^*(\tau) = \frac{1}{2}R_S^{*2}(\tau) \left\{ 2\arcsin\left(\frac{W_S^*(\tau)}{2R_S^*(\tau)}\right) - \sin\left[2\arcsin\left(\frac{W_S^*(\tau)}{2R_S^*(\tau)}\right)\right]\right\}, \tag{3.3}$$

where the dimensionless instantaneous central sheet width $W_S^*(\tau)$ can be calculated from

$$W_S^*(\tau) = 2\sqrt{R^{*2}(\tau) - (\Delta x^*/2)^2}. \tag{3.4}$$

The thickness of the spreading lamella varies across the spread radius and evolves temporally (Roisman *et al.* 2009; Gordillo *et al.* 2019). Figure 10(c) shows a simplified schematic for the temporal evolution of the thickness of the lamella segments, whose bottom views are shown in figure 10(a). For a lamella segment, $T_{LS}(r, t)$ represents the local instantaneous lamella thickness at radial distance r and time t. From the morphology of the impact processes demonstrated in §3.2, it is evident that the interaction usually occurs at the outer lamella portions where the liquid spreads radially on the impact surface,
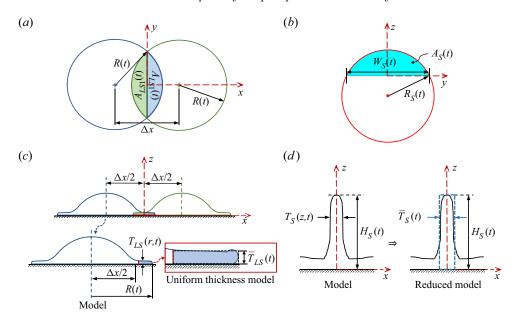
961 A17-16

Figure 10. (*a*) Schematic of the geometry of the contact lines of the interacting lamellae on the impact surface (at x–y plane). The shaded areas ($A_{LS1}(t)$) represent the lamella segments that contribute to the central sheet formation at the intersection line at each time. (*b*) Schematic of the geometry of the 'semilunar' central sheet (shaded area) with the fitted circle (at the y–z plane). The variables $W_S(t)$, $A_S(t)$ and $R_S(t)$ represent respectively the sheet width, the sheet area and the radius of curvature of the sheet. (*c*) Schematic for the modelling of the instantaneous uniform thickness of the lamella segments, $\bar{T}_{LS}(t)$ (at the x–z plane). The central sheet is not shown for a simplified schematic representation. (*d*) Schematic for the modelling of the instantaneous uniform thickness of the central sheet $\bar{T}_S(t)$ (at the x–z plane). Here, $H_S(t)$ indicates the instantaneous height of the central sheet.

and the variation of thickness is quite small at these outer slender lamella segments. Therefore, the variation in the lamella thickness $T_{LS}(r, t)$ along the radial direction can be neglected and we can consider an average lamella thickness $\bar{T}_{LS}$ at each time, as shown in the magnified lamella segment of figure 10(*c*). Accordingly, $\bar{T}_{LS}$ can be evaluated as

$$\bar{T}_{LS}(t) = \frac{1}{\left(R(t) - \dfrac{\Delta x}{2}\right)} \int_{x=\Delta x/2}^{x=R(t)} T_{LS}(x, t)\, \mathrm{d}x. \tag{3.5}$$

Figure 10(*d*) shows a schematic of the vertical growth of the central sheet, whose 'semilunar' side view is shown in figure 10(*b*) and quantified in figure 9. In figure 10(*d*), $H_S(t)$ is the instantaneous maximum sheet height at time t and $T_S(z, t)$ is the instantaneous thickness of the sheet at vertical distance z and time t. From the morphological demonstration, it is also evident that the variation of thickness along the vertically rising central sheet is not significant. Therefore, the variation in sheet thickness $T_S(z, t)$ along the z-axis can be neglected, and a uniform sheet thickness $\bar{T}_S$ can be defined at each time as

$$\bar{T}_S(t) = \frac{1}{H_S(t)} \int_0^{H_S(t)} T_S(z, t)\, \mathrm{d}z. \tag{3.6}$$

The reduced model of the vertically ascending central sheet with its uniform thickness $\bar{T}_S(t)$ is also shown in figure 10(*d*).

Considering the geometrical description of the impact process, i.e. the liquid of the shaded lamella segments contributes to the vertical central sheet formation, and assuming a uniform thickness of the lamella segments at each time, a simplified mass balance can approximate the uniform central sheet thickness as $\bar{T}_S(t) \approx A_{LS}(t)T_{LS}(t)/A_S(t)$. Thus, using (3.2) and (3.3), the dimensionless instantaneous uniform central sheet thickness $T_S^*(= \bar{T}_S/D_0)$ can be determined at each time as

$$T_S^*(\tau) = \frac{2T_{LS}^*(\tau)R^{*2}(\tau)\left\{2\arccos\left(\frac{\Delta x^*}{2R^*(\tau)}\right) - \sin\left[2\arccos\left(\frac{\Delta x^*}{2R^*(\tau)}\right)\right]\right\}}{R_S^{*2}(\tau)\left\{2\arcsin\left(\frac{W_S^*(\tau)}{2R_S^*(\tau)}\right) - \sin\left[2\arcsin\left(\frac{W_S^*(\tau)}{2R_S^*(\tau)}\right)\right]\right\}}, \quad (3.7)$$

where the dimensionless instantaneous uniform lamella thickness $T_{LS}^*(\tau) = \bar{T}_{LS}(t)/D_0$.

Equations (3.2)–(3.7) apply only to the ascending motion of the central sheet. These equations are not expected to describe the behaviour of a central sheet during its descent. Also, these equations aim to describe the vertical sheet evolution for sufficiently large inter-droplet spacing (e.g. not for $\Delta x^* = 1.32$, which leads to the non-semilunar ascending sheet, as discussed in § 3.2.2).

The measured temporal evolution of the central sheet and the temporal spread of the liquid on the impact surface is presented in § 3.4 for different impact parameters and compared to the geometrically estimated values of the central sheet characteristics (e.g. sheet width and sheet thickness).

3.4. *Quantitative analysis of surface liquid spread and central sheet growth*

Several image analysis algorithms were implemented in MATLAB to quantify the instantaneous characteristics of the central sheet, as illustrated in figure 11, from the sequential front- and side-view images. As shown from both front and side views, the height of the sheet H_S represents the maximum height across the sheet and is crucial in dictating the sheet rim instability. The spread of the combined liquid mass on the impact surface, as illustrated earlier in figure 6(*a*), can be characterised by three parameters: the front spread length (S_{Lx}), the side spread length or diameter (S_{Ly}) and the sheet width (W_S), shown in figure 11. The radial contact line velocities of the left and right spreading lamellae are represented by V_{LL} and V_{LR}, respectively (figure 11), and their temporal evolution can be determined from their time-dependent spread radius. Similarly, the velocity of the uprising sheet (V_S) can be determined from the temporal upwards rise of the sheet. All illustrated measured parameters of figure 11 are reported dimensionless by the initial droplet diameter (D_0) as the length scale and the droplet impact velocity (V_0) as the velocity scale.

3.4.1. *Central sheet height*

Figure 12(*a*) shows the temporal variation of the dimensionless central sheet height H_S^* ($= H_S/D_0$) for four different impact *We* (see figures 4 and 5 for related morphology). For all cases, H_S^* initially increases rapidly with τ, then slowly reaches a maximum value, and subsequently, H_S^* decreases with τ but at a slower rate than its growth phase. However, H_S^* appears to depend appreciably on *We* since higher *We* leads to increased available liquid kinetic energy to assist higher and prolonged growth of the central sheet. For example, for impact with $We = 54$, H_S reaches the peak value of $\approx 0.76D_0$ at $\tau \approx 1.75$, whereas for impact with $We = 128$, H_S reaches the peak value of $\approx 1.32D_0$ at $\tau \approx 2.5$ (figure 12*a*).
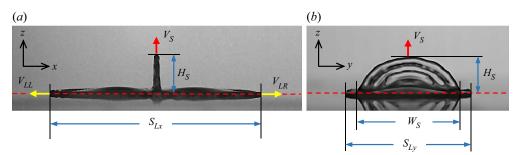
Figure 11. Definition of sheet characteristics in the (*a*) front- and (*b*) side-view images, including the central sheet height (H_S), the combined liquid front spread length (S_{Lx}), the combined liquid side spread length (S_{Ly}) and the central sheet width (W_S) at a time t after impact. Along with the yellow arrows, V_{LL} and V_{LR} represent the advancing velocity of the left and right lamella, respectively. Similarly, V_S represents the velocity of the uprising sheet. The red dashed line on each image represents the impact surface line.

As the sheet grows both laterally and upwardly with time, its growth is decelerated by the effect of gravity and surface tension. The kinetic energy of the liquid mass contributes to the sheet's surface energy (S_E) and gravitational potential energy (P_E). We estimate the instantaneous surface energy of the sheet as $S_E(t) = \sigma(2A_S(t) + l_S(t)\bar{T}_S(t))$, where the first term inside the parentheses approximates the instantaneous total side area of the sheet, and the second term approximates the instantaneous surface area of the sheet's circular boundary with $l_S(t)$ as the instantaneous arclength of the sheet segment. The potential energy of the sheet is estimated at each time as $P_E(t) = m_S(t)gz_S(t)$, where $m_S(t)(= \rho gA_S(t)\bar{T}_S(t))$ is the instantaneous mass of the sheet, g is the gravitational acceleration and $z_S(t)$ is the instantaneous height of the sheet centroid. We define a sheet energy ratio as $E_R = S_E/P_E$, which evaluates the relative magnitude of the two contributions. The temporal variation of E_R is shown in figure 12(*b*) for the impact processes evaluated in figure 12(*a*). Figure 12(*b*) considers only the sheet's ascending phase; therefore, the variation of E_R is presented up to the time of the maximum H_S^* for a given *We*. For all cases, the surface energy remains at least one order of magnitude larger than the potential energy throughout the vertical ascent although the difference decreases with time (figure 12*b*). Therefore, for the considered range of *We*, surface tension is mainly responsible for the deceleration of the vertically ascending sheets as opposed to gravity.

Figure 13(*a*) shows the temporal variation of the dimensionless sheet height (H_S^*) for four inter-droplet spacings (see figures 7 and 8 for related morphology). In figure 13(*a*), the peak value of H_S^* increases monotonically from ≈ 0.57 to ≈ 0.96 when Δx^* is reduced from 2.25 to 1.64. In addition, the dimensionless time τ of the peak H_S^* decreases monotonically from ≈ 2.24 to ≈ 1.91 for the same range of Δx^*. The temporal variation of H_S^* for $\Delta x^* = 2.25$, 1.96 and 1.64 follows a similar trend to that for different *We* in figure 12(*a*). However, a further decrease to $\Delta x^* = 1.32$ results in a unique variation of H_S^* with τ. As explained earlier, for $\Delta x^* = 1.32$, the central sheet becomes significantly stretched, resembling a nearly rectangular shape, due to its dominant lateral expansion. Consequently, its ascent motion stops suddenly at $\tau \approx 1$ at a peak H_S^* of ≈ 0.9, which is even lower than the peak H_S^* for the higher Δx^* of 1.64. In addition, unlike all other cases, for $\Delta x^* = 1.32$, the central sheet retains an average H_S^* value close to its peak for the time interval $1 < \tau < 3.4$ before its monotonic reduction. The variation H_S^* for $1 < \tau < 3.4$ is a consequence of the temporal evolution of the unique horn-like structures at the two ends of the descending sheet (see figure 8 for related morphology). Figure 13(*b*) shows the temporal variation of the energy ratio E_R of the 'semilunar' ascending sheets for different
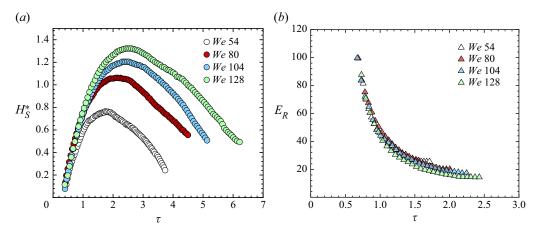
961 A17-19

Figure 12. (*a*) Variation of the dimensionless central sheet height ($H_S^* = H_S/D_0$) with dimensionless time ($\tau = tV_0/D_0$) for different impact Weber numbers (*We*). Here, H_S is defined in figure 11. The inter-droplet spacing is constant at 5.65 ± 0.15 mm ($\Delta x^* = 1.80 \pm 0.03$). (*b*) Temporal variation of the energy ratio $E_R (= S_E/P_E)$ up to the time of the peak height of the vertically ascending central sheets of panel (*a*). Here, S_E is the surface energy and P_E is the potential energy of the ascending sheets.
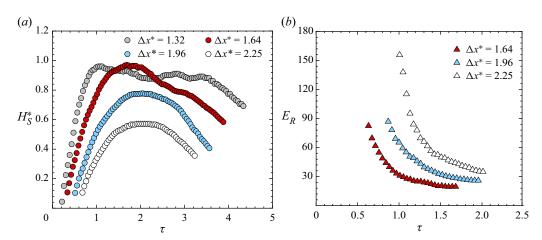

Figure 13. (*a*) Variation of the dimensionless central sheet height ($H_S^* = H_S/D_0$) with the dimensionless time (τ) for different dimensionless inter-droplet spacings ($\Delta x^* = \Delta x/D_0$). Here, H_S is defined in figure 11. The Weber number is constant at 62 ± 1. (*b*) Temporal variation of the energy ratio $E_R (= S_E/P_E)$ up to the time of the peak height of the vertically ascending central sheets of panel (*a*).

Δx^*, except for $\Delta x^* = 1.32$ (the sheet takes a 'rectangular' shape for this case). Similar to the observations for different *We*, figure 13(*b*) shows that the surface energy is at least one order of magnitude higher than the potential energy throughout the sheet ascent, and the dominance of the surface energy becomes more pronounced with increasing inter-droplet spacing, i.e. for the sheets with relatively lower H_S^*.

The momentum transfer from each lamella at the instant of the first lamella–lamella interaction depends on the radial speed of the lamella $V_L = dR/dt$ at the spread radius $R = \Delta x/2$ (see figure 14*a*). The radial spreading of the lamellae is decelerated with time and distance due to surface tension and viscous stresses. For a given droplet impact *We*, Δx determines the lamella expansion speed V_L at $\tau = \tau_0$ and *vice versa*. Here, V_L right
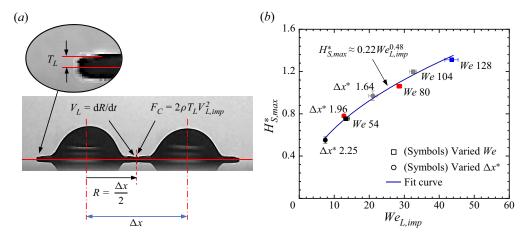
961 A17-20

Figure 14. (*a*) Front view of the collision of two lamellae, with the definition of the collision force F_C per unit arclength, lamella edge velocity V_L and thickness T_L. (*b*) Maximum non-dimensional sheet height $H^*_{S,max}$ ($= H_{S,max}/D_0$) as a function of the lamella impact Weber number $We_{L,imp}$ ($= F_C/\sigma$) for different impact conditions. Square symbols correspond to varied *We* cases, and circles correspond to varied Δx^* cases, as marked next to the symbols. Error bars represent the standard deviation. The solid line is the best-fit scaling law ($H^*_{S,max} \sim We^{0.48}_{L,imp}$) for the considered conditions.

before the lamella–lamella impact determines the initial uprising sheet velocity, i.e. the initial sheet velocity is higher for higher V_L at $\tau = \tau_0$ (see Appendix A for related lamella velocity and sheet velocity variation). At $\tau = \tau_0$, the lamella–lamella collision momentum is proportional to the inertia of the lamella edges. We consider a lamella–lamella impact force per unit arclength of the lamella edges as $F_C = 2\rho T_L V^2_{L,imp}$, where T_L is the average thickness of the lamella edges and $V_{L,imp} (= V_L)$ is the lamella–lamella impact velocity at $\tau = \tau_0$ (figure 14*a*). Upon lamella–lamella impact, a central sheet expands vertically in quiescent air without interacting with any solid surface, such as forming a viscous boundary layer, and therefore, its expansion is nearly inviscid. Also, gravity marginally contributes to the dynamics of 'semilunar' central sheets, as discussed above. Therefore, the central sheet dynamics is primarily governed by the inertia at the lamella–lamella impact and surface tension.

We define a dimensionless lamella impact Weber number as the ratio of the collision force (the rate of change of momentum) per unit arclength and surface tension as $We_{L,imp} = F_C/\sigma = 2\rho T_L V^2_{L,imp}/\sigma$. We plot the dimensionless maximum sheet height $H^*_{S,max}$ ($= H_{S,max}/D_0$) versus $We_{L,imp}$ in figure 14(*b*) for all cases of impact *We* (figure 12*a*) and of Δx^* (figure 13*a*), except for $\Delta x^* = 1.32$ due to the 'non-semilunar' sheet evolution for that case. Figure 14(*b*) shows the best-fit scaling as $H^*_{S,max} \approx 0.22 We^{0.48}_{L,imp}$, with an R-squared value of 0.99. The obtained scaling law, $H^*_{S,max} \sim We^{0.48}_{L,imp}$, follows nearly a square-root dependence on the lamella–lamella impact Weber number. This dependence is reminiscent of the square-root scaling law for the maximum horizontal spread factor $\beta_{max} \sim We^{1/2}$ (Bennett & Poulikakos 1993; Eggers *et al.* 2010; Josserand & Thoroddsen 2016) for a single-droplet impact on a solid surface, obtained by disregarding viscous dissipation and considering a balance between the inertial and surface tension forces. In addition, for the impact of a single droplet on different geometries, namely on small targets (Rozhkov, Prunet-Foch & Vignes-Adler 2004; Villermaux & Bossa 2011; Vernay, Ramos & Ligoure 2015) or close to the straight edge of a substrate (Lejeune *et al.* 2018),
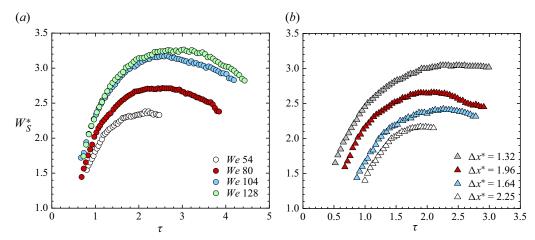
Figure 15. Temporal evolution of the dimensionless sheet width ($W_S^* = W_S/D_0$): (*a*) for different Weber numbers (*We*); and (*b*) for different dimensionless inter-droplet spacings ($\Delta x^* (= \Delta x/D_0)$). Here, Δx^* is fixed at ≈ 1.80 for panel (*a*), whereas *We* is constant at ≈ 62 for panel (*b*).

a scaling of the maximum sheet extension with $We^{1/2}$ has also been found for 'inviscid' horizontal liquid sheets (i.e. sheets that are not adjacent to a solid surface and expand horizontally in air). Thus, by analogy to the scaling of the maximum sheet extension with $We^{1/2}$ for 'inviscid' horizontal sheets for single-droplet impacts, the obtained scaling law for the lamella–lamella impact is a reasonable approximation for the maximum central sheet height for droplet-pair impacts.

3.4.2. *Central sheet width*

The temporal evolution of the central sheet width W_S (defined in figure 11) is crucial for the formation of the liquid sheet. Figure 15 shows the effect of impact *We* and inter-droplet spacing Δx^* on the temporal variation of $W_S^* (= W_S/D_0)$. Figure 15(*a*) compares the sheet evolutions of figure 5 and shows that W_S^* increases appreciably with increasing impact *We*. For all cases, W_S^* increases up to a maximum value during the rise of the central sheet and then starts to decrease as the sheet falls back on the receding lamellae. Similarly, figure 15(*b*) shows that W_S^* depends strongly on Δx^* and W_S^* increases appreciably with decreasing Δx^* (see figure 8 for related morphology). Figure 16 demonstrates good agreement between the measurements of $W_S^*(\tau)$ and the estimation by (3.4) for the ascending motion of the central sheet for a wide range of impact conditions.

3.4.3. *Spread of the combined liquid mass*

During the evolution of the central sheet, the area of the combined liquid mass on the impact surface resembles two truncated spreading lamellae connected at the base of the sheet, as shown schematically in figure 6(*a*). This area resembles an approximate 8-shape at the start of the central sheet generation, connecting two lamella circles with quite a short sheet base. Figure 17 shows the temporal evolution of the dimensionless front spread length ($S_{Lx}^* = S_{Lx}/D_0$) and side spread length ($S_{Ly}^* = S_{Ly}/D_0$) of the combined liquid mass for the varied *We* (figure 17*a*,*b*) and Δx^* (figure 17*c*,*d*) cases. The front spread length S_{Lx} and the side spread length S_{Ly} have been defined in figure 11.
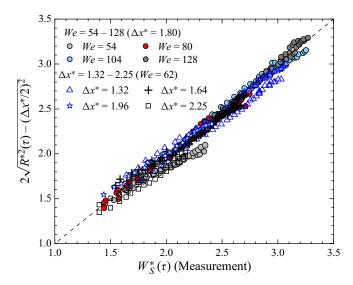
961 A17-22

Figure 16. Comparison between the dimensionless instantaneous central sheet width $W_S^*(\tau)$ estimated by (3.4) and the corresponding measured value for different impact conditions presented in figure 15. For all cases, $W_S^*(\tau)$ is considered only for the ascending motion of the central sheet, i.e. for $H_S^*(\tau) \leq H_{S,max}^*$, where $H_{S,max}^*$ represents the maximum $H_S^*(\tau)$ for a given impact process.

For a fixed Δx^*, the combined liquid area increases with increasing We, as depicted by the temporal variation of S_{Lx}^* and S_{Ly}^* (figure 17a,b). At any time, S_{Lx}^* and S_{Ly}^* can be theoretically expressed as $2R^*(\tau) + \Delta x^*$ and $2R^*(\tau)$, respectively (see figure 6 for a related schematic). In figure 17(a,b), we compare the experimental S_{Lx}^* and S_{Ly}^* to their respective theoretical expression. The dashed lines correspond to the theoretical expression for $R^*(\tau)$ of (3.1) (i.e. based on Roisman *et al.* 2002) while the solid lines correspond to the theory of Gordillo *et al.* (2019). Similar to observations for the spread radius in figure 3, the theoretical evaluations with $R^*(\tau)$ from Gordillo *et al.* (2019) are in excellent agreement with our measurements. It is noted that the theoretical prediction considers an advancing lamella up to its maximum spread. Thus, a deviation of the theoretical line from the experimental data is not surprising at the later receding stage of the lamellae. However, for a fixed We, as expected, S_{Lx}^* increases with increasing Δx^*, and S_{Ly}^* remains almost invariant with Δx^* due to the constant impact We (figure 17c,d). It is noted that the first instant of the lamella interaction (τ_0) varies with Δx^*, and correspondingly, the evolution curve of the combined liquid mass starts later for higher Δx^* (figure 17c,d). Similar to the different We cases (figure 17a,b), the theoretical evaluation shows a good agreement with our experimental measurements when $R^*(\tau)$ is from Gordillo *et al.* (2019), as shown in figure 17(c,d). In effect, figure 17 also confirms that the spreading of the lamellae away from the collision line region remains unaffected by the collision.

3.4.4. *Central sheet area and thickness*
The instantaneous lamella segment area ($A_{LS}^*(\tau)$) that contributes to the central sheet evolution and the dimensionless area of the ascending central sheet ($A_S^*(\tau)$) have been estimated by (3.2) and (3.3), respectively (see the related schematic in figure 10). These two areas are compared in figure 18(a), and it seems that $A_{LS}^*(\tau)$ and $A_S^*(\tau)$ are comparable
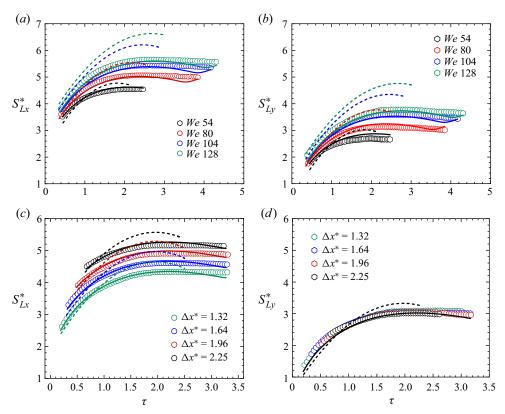
Figure 17. Temporal evolution of the dimensionless front spread length (S_{Lx}^*) and the dimensionless side spread length or diameter (S_{Ly}^*) of the combined liquid mass for (*a,b*) different impact Weber number *We* and (*c,d*) dimensionless inter-droplet spacing Δx^* cases. Here, S_{Lx}^* and S_{Ly}^* are compared with the corresponding theoretical expressions $2R^*(\tau) + \Delta x^*$ and $2R^*(\tau)$, respectively. The solid lines correspond to the theoretical expressions evaluated with $R^*(\tau)$ obtained by Gordillo *et al.* (2019), and the dashed lines correspond to the same obtained by (3.1) (Roisman *et al.* 2002). The theoretical lines' colour is the same as the corresponding experimental symbols' edge colour.

to each other for a wide range of impact conditions. This scenario indicates that the instantaneous central sheet thickness ($T_S(r, t)$) depends primarily on the instantaneous thickness of the lamella segments ($T_{LS}(r, t)$). From the front-view images, the average thickness of the lamella segments ($\bar{T}_{LS}(t)$), defined in (3.5)) that contribute to the central sheet, can be determined from the unaffected side of the two lamellae, as shown in figure 18(*b*). By using an image analysis algorithm, for both spreading lamellae (left and right), $\bar{T}_{LS}$ has been measured at each time from $x = \Delta x/2$ to $x = R(t)$.

From the front-view images of the central sheet evolution, the instantaneous average thickness of the uprising central sheet ($\bar{T}_S(t)$, defined in (3.6)) has been quantified through image analysis. An estimation of the dimensionless instantaneous average volume of the uprising central sheet is made by $A_S^*(\tau) \times T_S^*(\tau)$, where $T_S^*(\tau) = \bar{T}_S(t)/D_0$. Similarly, the corresponding dimensionless instantaneous average volume of lamella liquid entering the central sheet is estimated by $A_{LS}^*(\tau) \times T_{LS}^*(\tau)$, where $T_{LS}^*(\tau) = \bar{T}_{LS}(t)/D_0$. Figure 18(*c*) compares the temporal evolution of these two estimated instantaneous average volumes for different impact processes. In effect, figure 18(*c*) compares the liquid mass of an uprising central sheet with the corresponding liquid mass of the lamella segments that contribute
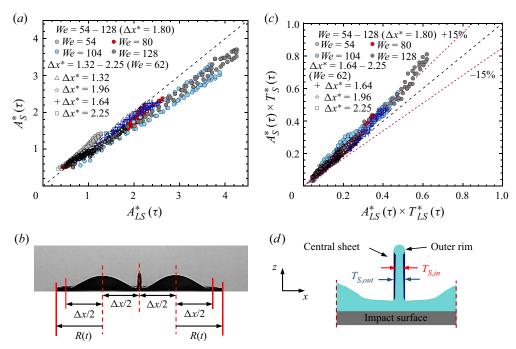
961 A17-24

Figure 18. (*a*) Comparison of the dimensionless instantaneous lamella segment area $A_{LS}^*(\tau)$ that contributes to the central sheet with the dimensionless instantaneous area of the ascending central sheet $A_S^*(\tau)$. Here, $A_{LS}^*(\tau)$ and $A_S^*(\tau)$ are estimated by (3.2) and (3.3), respectively. (*b*) Schematic for the determination of the instantaneous average thickness of the lamella segments ($\bar{T}_{LS}(t)$). (*c*) Comparison of the dimensionless instantaneous average volume of the uprising central sheet $A_S^*(\tau) \times T_S^*(\tau)$ with the dimensionless instantaneous average volume of the lamella liquid entering the sheet $A_{LS}^*(\tau) \times T_{LS}^*(\tau)$. Here, $T_S^*(\tau)$ and $T_{LS}^*(\tau)$ respectively represent the dimensionless instantaneous average central sheet thickness and the dimensionless instantaneous average thickness of the lamella segments contributing to the sheet. (*d*) A simplified schematic of the cross-section of a rim-bounded central sheet (at the *x–z* plane). Here, $T_{S,out}$ and $T_{S,in}$ respectively represent the thickness of the outer rim and the inner sheet portion.

to the central sheet growth. Figure 18(*c*) shows a good balance between the instantaneous liquid masses of the central sheet and the instantaneous contribution from the expanding lamellae. However, the estimated temporal mass of the central sheet tends to be larger than that of the estimated temporal liquid mass entering the sheet. It is noted that the thickness of an uprising central sheet at its outer rim portion ($T_{S,out}$) can differ from its thickness at the inner sheet portion ($T_{S,in}$), as the rim can gradually become thicker relative to the inner sheet portion (see figure 18*d*). Therefore, by analysing the front-view images for all cases of figure 18(*c*), the projection of the peripheral sheet rim thickness (i.e. $T_{S,out}$) is averaged in estimating $T_S^*(\tau)$, leading to an unsurprising overestimated mass of the central sheet, as reflected in figure 18(*c*). It is noted that the central sheets for $\Delta x^* = 1.32$ are not considered for thickness quantification as the obtained front-view images of these sheets reveal their non-orthogonal evolution with respect to the front plane of the imaging camera (see figure 7 for a typical example of the obtained sheet morphology for $\Delta x^* = 1.32$). Figure 19 compares the measured dimensionless instantaneous central sheet thickness ($T_S^*(\tau)$) with the estimation by (3.7), and a good agreement is found for the considered impact conditions.
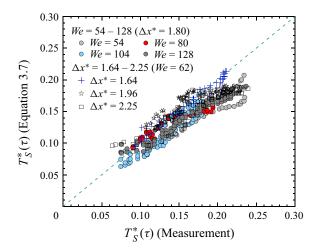
Figure 19. Comparison between the dimensionless instantaneous central sheet thickness $T_S^*(\tau)$ estimated by (3.7) and the corresponding measured value for different impact Weber numbers (*We*) and dimensionless inter-droplet spacing (Δx^*). For all cases, $T_S^*(\tau)$ is considered only for the ascending central sheet, i.e. $H_S^*(\tau) \leq H_{S,max}^*$, where $H_{S,max}^*$ represents the maximum $H_S^*(\tau)$ for a given case.

3.5. *Central sheet splashing*

To characterise the central sheet formation and growth, the inter-droplet spacings and impact Weber numbers of this study were deliberately chosen to inhibit sheet splashing. For instance, for $\Delta x^* \approx 1.80$, splashing from an uprising central sheet was not observed for $We \lesssim 128$ (see figures 4 and 5 for the related morphology). However, as the impact *We* was further increased for $\Delta x^* \approx 1.80$, splashing becomes evident from the central sheet for $We \approx 155$ (figure 20), while a single-droplet impact at these conditions does not lead to splashing. Figure 20 and the supplementary movie 10 depict the morphology of splashing for a droplet-pair impact ($\Delta x^* \approx 1.80$ and $We \approx 155$) and only surface deposition for an equivalent single-droplet impact.

For the droplet-pair impact, instability-driven cusps become evident at the ascending central sheet rim at $\tau \approx 1.5$ (figure 20). Subsequently, several finger-like jets protrude from these cusps almost symmetrically, with one in the middle. The protruding jets grow with time and may disintegrate into secondary droplets, as observed for $\tau \approx 2.5$ (figure 20). Also, merging of adjacent jets and rim-tearing appear at several points of the sheet rim, leading to a rapid vertical descent of the inner sheet portion and the formation of two analogous liquid ligaments at the sheet side ends. The liquid side-ligaments are appreciably large compared to the earlier protruding jets, and eventually, the disintegration of these ligaments yields two large secondary droplets (figure 20). Therefore, the source of secondary droplets during a central sheet splashing can be the earlier protruding non-merged jets and the later formed relatively thick ligaments. We quantified the breakup time of the central sheet of figure 20 relative to the time of the first interaction of two lamellae. The two lamellae first interact at time $t = 0.56$ ms, and the breakup of the first finger-like jet occurs at $t = 4.44$ ms, leading to a sheet breakup time of 3.88 ms. This breakup time includes the time for the development of the sheet and the subsequent instability-driven finger-like jet till the first secondary droplet detachment. Similarly, the sheet lifetime, i.e. the time from the first lamella interaction till the final thick ligament breakup, is found to be ≈ 11.67 ms, which is close to the capillary time of the impacting
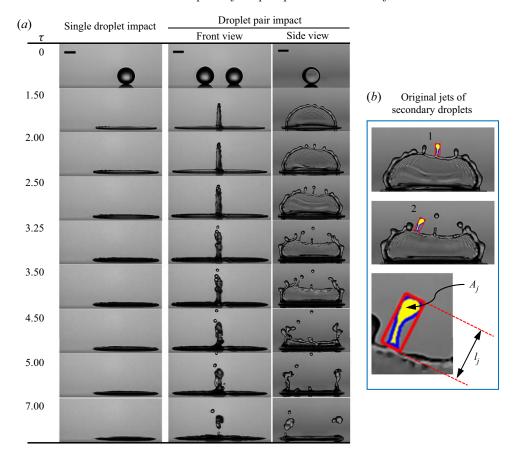
Figure 20. Impact process for a single-droplet impact and a droplet-pair impact on the acrylic surface ($We \approx$ 155 for both cases, and $\Delta x^* \approx 1.80$ for the droplet pair). Scale bars are 2 mm. The detection of the jets that lead to secondary droplet and the associated jet parameters are shown inside the blue boundary in panel (*b*). Here, A_j is the projected area and l_j is the length of the jet. See supplementary movie 10 for the corresponding video.

droplet $t_c = \sqrt{4\rho(D_0/2)^3/(3\sigma)} \approx 9\,\mathrm{ms}$, similar to that observed for the horizontally expanding sheet in air (Lejeune *et al.* 2018).

However, for the case of the equivalent isolated single-droplet impact ($We = 155$), the bulk liquid spreads on the impact surface with a perturbed rim and deposits with no prompt and/or delayed splash (figure 20). The splashing threshold for a single-droplet impact can be characterised by the so-called 'splashing parameter' $K = Oh^{-0.4}We$, where the dimensionless Ohnesorge number is $Oh = \mu/\sqrt{\rho D \sigma}$. On a smooth surface, splashing happens if K exceeds a critical value (K_S) as (Cossali, Coghe & Marengo 1997)

$$K_S = 649 + 3.76/R_a^{*0.63}, \tag{3.8}$$

where R_a^* represents the dimensionless roughness amplitude, i.e. $R_a^* = R_a/D_0$. The acrylic surface of the present study has a roughness amplitude (R_a) of 1.17 nm resulting in $K_S = 42\,765$, which is one order of magnitude larger than the K parameter ($K = Oh^{-0.4}We = 1820$) of the impact process. Hence, for the single-droplet impact of figure 20, splashing (prompt or delayed) is neither expected (Cossali *et al.* 1997) nor observed. In contrast,

961 A17-27

splashing is observed for the same impact Weber number due to the breakup of the central sheet formed during droplet-pair impacts. The findings of the present study confirm and quantify the suggestion that the interaction of two droplets can lead to splashing (Roisman *et al.* 2002).

In the literature, the detachment of droplets from jets is commonly attributed to Rayleigh breakup (Rayleigh 1878; Cossali, Marengo & Santini 2004) and 'end-pinching' (Schulkes 1996; Gordillo & Gekle 2010; Hoepffner & Paré 2013; Wang *et al.* 2018; Wang & Bourouiba 2021) of the jets. The Rayleigh breakup occurs due to the RP instability of the fastest growing mode, whereas the end-pinching occurs due to the retraction of the jet tips (Wang *et al.* 2018). In both cases, the size of a jet-detached secondary droplet is proportional to the width of the jet. For the Rayleigh breakup of a jet, the droplet-jet size ratio is given by $\varepsilon_{RP} = d/w = 1.89$, where d is the secondary droplet diameter and w is the width of the jet that ejects the secondary droplet (Rayleigh 1878). In contrast, for the end-pinching of a jet, the associated droplet-jet size ratio $\varepsilon_{EP}(= d/w)$ is 1.5 to 1.6, and ε_{EP} is independent of the impact *We* and the time of the droplet detachment (Schulkes 1996; Wang *et al.* 2018). For a droplet-pair impact with $\Delta x^* \approx 1.80$ and $We \approx 155$ (of figure 20), we measured the diameter d of each secondary droplet shed from a non-merged jet using $d = \sqrt{4A_d/\pi}$, where A_d is the projected area of the secondary droplet in a processed image. It is noted that, following the detachment, a secondary droplet oscillates along its trajectory under the balance of its surface tension and inertia. Therefore, for each secondary droplet, we measured d for ten consecutive images, starting with the first image of the droplet detachment. The diameter measurement of the oscillating secondary droplets resulted in a maximum standard deviation of less than 7 %. We determined the length (l_j) and width (w) of the jets of origin of the secondary droplets with an image analysis program (incorporating image erosion, dilation and subtraction) to detect and isolate any peripheral jet of interest from the central sheet and fit a bounding rectangle around the jet. The jet length l_j is determined from the bounding rectangle and the average jet width is determined over its length as $w = A_j/l_j$ (see figure 20). For the droplet-pair impact of figure 20, we find two secondary droplets with d of 0.64 ± 0.04 mm and 0.77 ± 0.03 mm respectively detaching at $\tau \approx 2.5$ and $\tau \approx 3.25$ from their original jets possessing w of 0.40 mm and 0.41 mm, respectively. Correspondingly, for this impact case, over the central sheet splashing period, we find $\varepsilon = d/w \approx 1.7$. Following this approach for a sample size of $N = 5$ for $\Delta x^* \approx 1.80$ and $We \approx 155$, we obtain the mean droplet-jet ratio as $\langle \varepsilon \rangle = d/w \approx 1.72$, which is between the predicted values of the droplet-jet ratio for the end-pinching (i.e. ε_{EP}) and the Rayleigh breakup (i.e. ε_{RP}). Depending on the image processing parameters, the uncertainty of the obtained value of $\langle \varepsilon \rangle$ is ± 4 % (see Appendix B for details). It is noted that the fastest growing mode of RP instability typically triggers the droplet detachment in the case of a long cylindrical jet, and the Rayleigh breakup strictly holds for 'infinite or semi-infinite' jets (Rayleigh 1878; Wang *et al.* 2018). For a jet, the wavelength of the RP instability at its fastest-growing mode is $\lambda_{RP} = 4.5w$ (Rayleigh 1878), and the jet length l_j must be considerably longer than λ_{RP} for the Rayleigh breakup to apply. In comparison, for the finger-like jets of the central sheets (of figure 20), we find $l_j \approx 4.2w$, which is smaller than one wavelength of the RP instability (i.e. $l_j < \lambda_{RP}$). Therefore, the finger-like original jets of the secondary droplets are too short for the Rayleigh breakup to occur. Instead, the secondary droplets of figure 20 (see also supplementary movie 10) seem to be ejected as a consequence of the retraction of jet tips, i.e. via the 'end-pinching' mechanism, as reported in the prior studies (Schulkes 1996; Gordillo & Gekle 2010; Hoepffner & Paré 2013; Wang *et al.* 2018; Wang & Bourouiba 2021).

In the literature, the splashing is explored for single-droplet impacts on both small (Rozhkov *et al.* 2002; Villermaux & Bossa 2011; Wang & Bourouiba 2021) and large (Thoroddsen, Takehara & Etoh 2012; Riboux & Gordillo 2015; Burzynski *et al.* 2020) solid surfaces. The experiments on small surfaces are notably different from those on large surfaces. A droplet impact on small surfaces leads to a free liquid sheet that expands with no contact on a solid surface and eventually atomises in ambient air. However, the lamella expands on a solid surface, and subsequent gas cushioning and corona development are observed in the case of a droplet impact on a large surface (Moore, Whiteley & Oliver 2018; Burzynski *et al.* 2020). The droplet impacts of the present study are on a large solid surface. Therefore, we compare the splashing from a droplet-pair impact and that from a single-droplet impact on large surfaces in terms of the size of ejected secondary droplets as described below.

At any instant, the size of the secondary droplets can be characterised by the arithmetic mean diameter (d_{10}) of the ejected droplets as $d_{10} = (1/n) \sum_{i=1}^{=n} d(i)$, where n is the total number of detected secondary droplets. In this study, d_{10} is the mean value of the diameters of twenty secondary droplets ($n = 20$) detected during five droplet-pair impacts. It is noted that there are approximately 3–5 secondary droplets generated during each droplet-pair impact. For single-droplet impact on large surfaces, Burzynski *et al.* (2020) investigated d_{10} over the entire splashing process (prompt and corona splashing) and scaled d_{10} to a relatively constant value as $d_{10}/D_0 \approx 1.5 Re^{-1/2}$, where the dimensionless Reynolds number $Re = \rho V_0 D_0 / \mu$. The authors have demonstrated a good agreement of their semi-empirical scaling law with the prior experimental findings of Faßmann *et al.* (2013) and Thoroddsen *et al.* (2012). Zhang *et al.* (2021) also reported a similar scaling law as $d_{10}/D_0 \approx 2.58 Re^{-1/2}$, with a different pre-factor but of the same order of magnitude. For the droplet impact case of figure 20, we find $Re \approx 5850$, which leads to $d_{10} \approx 0.02 D_0$ and $d_{10} \approx 0.03 D_0$, respectively, from the scaling law of Burzynski *et al.* (2020) and of Zhang *et al.* (2021). Therefore, for splashing from a single-droplet impact with $Re \approx 5850$, we can expect secondary droplets with d_{10} roughly 2–3 % of the impacting droplet diameter D_0. In contrast, for the central sheet splashing for the droplet-pair impact (figure 20) with $Re \approx 5850$ ($We \approx 155$, $\Delta x^* \approx 1.80$), we find d_{10} of the secondary droplets that detach from the finger-like jets ranging between 22 % and 26 % of D_0. In addition, the thick ligaments that are detected later (figure 20 for $\tau = 7$) result in even larger droplets with d_{10} up to 50 % of D_0. Thus, it appears that central sheet splashing results in large secondary droplets with a dimensionless mean size (i.e. d_{10}/D_0) one order of magnitude larger than those observed for single-droplet impact. This finding can explain the origin of large secondary droplets during spray impact on surfaces. For spray impacts on solid surfaces, Roisman, Horvat & Tropea (2006) experimentally obtained a scaling law for d_{10} of the ejected secondary droplets as $d_{10}/D_0 \approx 11 Re^{-1/2}$, with a pre-factor that is one order of magnitude larger than that for single-droplet impact. It is noted that ejection of larger secondary droplets (with d_{10} up to 30 % of D_0) has also been observed for single-droplet impacts on small surfaces (Villermaux & Bossa 2011; Wang *et al.* 2018), a case different from our experimental case (i.e. droplet impact on a large surface). In summary, for droplet impacts on large solid surfaces, the interaction between droplet impacts assists the lowering of the splashing threshold and the generation of much larger secondary droplets during splashing than those from single-droplet impacts.

It is worth noting that the droplet-pair impact configuration of the present study is related to two additional configurations: (i) the simultaneous impact of twin droplets on a liquid pool (Artman-Breitung, Watson & Dickerson 2021); and (ii) the impact of a single droplet

close to the straight edge of a solid substrate (Lejeune *et al.* 2018; Lejeune & Gilet 2019). The former configuration can lead to the interaction of two crowns that form a central veil (or sheet), analogous to the central sheet here. Although the latter configuration involves a single-droplet impact, it yields a similar liquid sheet (with capillary waves, semilunar and rectangular shapes, sheet breakup in ligaments, and relatively large droplets). Similar variations in the expanding sheets' dynamics are observed based on the Weber number and the distance between the impact point and the sheet basis. The scaling law proposed here for the maximum sheet height is analogous to the maximum sheet extension of Lejeune *et al.* (2018). However, the key differences between both configurations are as follows. In the case of the central sheet of the current study, the liquid velocity changes direction from horizontal (in the lamella) to vertical (in the liquid sheet), while in the configuration of Lejeune *et al.* (2018) and Lejeune & Gilet (2019), the liquid velocity remains parallel to the substrate plane during the whole process. In addition, the liquid sheet here is fed by two interacting droplets instead of one in Lejeune's configurations. The presence of the horn-like shapes of the current study due to the combined effect of the closeness of the interacting droplets (i.e. for $\Delta x^* = 1.32$) and change of liquid velocity direction is absent from Lejeune's studies. Finally, the liquid mass of the vertical sheet can eventually deposit on the impact substrate here, unlike the eventual separation of the sheet and substrate for Lejeune's configurations.

4. Conclusions

The impact of multiple droplets onto solid surfaces is a ubiquitous yet not fully understood phenomenon. We studied the physics of the simultaneous impact of two droplets on a large solid surface through a combined experimental and theoretical investigation. We developed a novel on-demand droplet generator that can eject two equal-sized droplets simultaneously without generating any trailing droplets. Fine control of droplet size and droplet release allowed the replication of experimental events for different impact Weber numbers ($54 \leq We \leq 155$) and inter-droplet spacings ($\Delta x = 1.32D_0$ to $2.25D_0$, with D_0 as the initial droplet diameter). Based on the investigation of the impact processes, several conclusions can be drawn as follows.

For the considered impact conditions, while a single-droplet impact resulted in liquid deposition on the impact substrate, the impacts of two droplets led to an uprising central sheet, which can deposit or break into droplets. The uprising central sheets evolved in time with a regular rim-bounded 'semilunar' shape with sub-millimetre propagating waves across the sheet and instability cusps appearing at the sheet rim depending on the impact *We* and inter-droplet spacing Δx. The propagating waves are capillary waves which contribute to thickening the outer sheet rim without causing any 'flapping-instability' on the sheet. We found that the influence of gravity is negligible for the development of the semilunar-shaped ascending sheet. We also demonstrated that the destabilisation of the central sheet rim and the consequent rim corrugations are governed by a coupled Rayleigh–Taylor and Rayleigh–Plateau mechanism.

While the central sheet usually evolves due to lamella–lamella interaction, a small inter-droplet spacing can lead to the interaction of the descending drop regions, as demonstrated for $We = 62$ and $\Delta x = 1.32D_0$. Such drop–drop interaction led to a dominating lateral expansion of the sheet, yielding a 'rectangular' uprising sheet instead of the usual 'semilunar' shape. This 'rectangular' central sheet eventually led to the formation of two horn-like liquid structures at the two side ends of the sheet, a characteristic that delays the deposition of the sheet liquid and is identified for the first time.

The uprising motion of the 'semilunar' central sheet is nearly inviscid in air. The dimensionless maximum sheet height $H_{S,max}^*$ ($= H_{S,max}/D_0$) scales with the dimensionless lamella–lamella impact Weber number $We_{L,imp}$ as $H_{S,max}^* \sim We_{L,imp}^{0.48}$. This near square-root dependence is analogous to the scaling of the maximum expansion with $We^{1/2}$ for 'inviscid' liquid sheets expanding horizontally in air (Rozhkov *et al.* 2004; Vernay *et al.* 2015; Lejeune *et al.* 2018) and on solid surfaces (Bennett & Poulikakos 1993; Josserand & Thoroddsen 2016) during single-droplet impacts.

Increased *We* and/or increased Δx increases the spread of the combined liquid mass on the impact substrate. The measured spreading of the individual lamellae and the combined liquid mass agree well with available theoretical models while the best agreement was with the model of Gordillo *et al.* (2019). Considering the geometrical constraint of multiple droplet impacts (i.e. lamella spread radius, inter-droplet spacing) and mass balance, we developed a geometrical description of the temporal evolution of the area of the interacting lamella segments (3.2), and the width (3.4) and thickness (3.7) of the uprising central sheet. We found that the developed description is in good agreement with the measured liquid sheet characteristics.

The formation of the central sheet lowers the splashing threshold and generates larger secondary droplets than those observed for single-droplet impacts. The arithmetic mean diameter d_{10} of the ejected secondary droplets was up to 50 % of the initial droplet diameter D_0, whereas splashing from single-droplet impacts on large surfaces could result in d_{10} less than 10 % of D_0. Our findings also explain the proposed scaling law by Roisman *et al.* (2006) $d_{10}/D_0 \approx 11Re^{-1/2}$ for secondary droplets formed during spray impact on large solid surfaces. We showed that the ejection of secondary droplets does not occur due to Rayleigh breakup but via end-pinching of the retracting jets of the central sheet.

Overall, the developed experimental facility enabled controlled replication of simultaneous droplet impacts. Combining experiments and theoretical investigation, this study provides new understanding of the largely unknown splash/non-splash outcomes of simultaneous multi-droplet impacts, important for a wide range of processes related to natural, medical and industrial applications.

Author ORCIDs.
Anjan Goswami https://orcid.org/0000-0003-1999-0668.

Appendix A. Lamella contact line velocity and central sheet velocity variation

Figure 21 shows the temporal evolution of the dimensionless contact line velocity of the left and right advancing lamellae (i.e. V_{LL}^* and V_{LR}^*, respectively) and that of the dimensionless velocity of the vertically ascending central sheet (i.e. V_S^*) for different impact *We* (related morphology in figures 4 and 5). These velocities have been defined in figure 11 and are normalised by the droplet impact velocity (V_0), i.e. for any velocity, $V^* = V/V_0$. Figure 21 shows that the lamella velocities V_{LL}^* and V_{LR}^* decrease with τ by viscous and surface tension effects. The momentum at the instant of the first lamella interaction (i.e. $\tau = \tau_0$) is higher for higher impact *We* due to the higher lamella velocities.
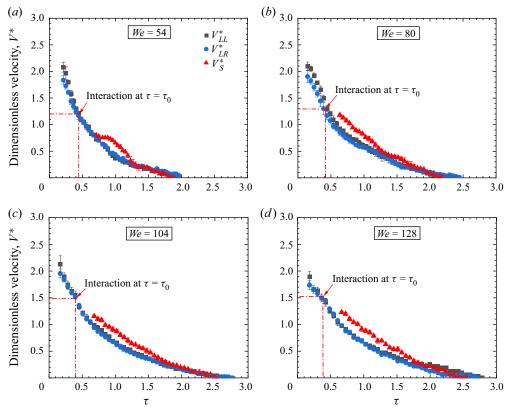
Figure 21. (*a–d*) Temporal evolution of the dimensionless contact line velocity of the left and right advancing lamellae (i.e. V_{LL}^* and V_{LR}^*, respectively) and the dimensionless velocity of the central uprising sheet (V_S^*) for different impact Weber numbers (*We*). All these velocities have been defined in figure 11. Here, τ_0 is the dimensionless time when two spreading lamellae start to interact. The inter-droplet spacing is constant at 5.65 ± 0.15 mm ($\Delta x^* = 1.80 \pm 0.03$). Error bars represent the standard deviation around the mean.

For all cases, the central sheet velocity V_S^* is comparable to the lamella contact line velocities V_{LL}^* and V_{LR}^*, and the sheet attains a zero velocity nearly at the dimensionless time when the contact lines reach their maximum spreads. Similar sheet velocity variation is also reported by Ersoy & Eslamian (2020) for droplet impacts on glass and Teflon substrates with an impact $We = 115$ and $\Delta x^* = 2.22$, which are different but within the ranges of the present study.

Figure 22 shows the variation of the dimensionless velocities for different inter-droplet spacing. For $\Delta x^* = 2.25$, 1.96 and 1.64, V_S^* decreases with τ, maintaining a similarity with the corresponding decrease in V_{LL}^* and V_{LR}^* (figure 22*a–c*). Conversely, for $\Delta x^* = 1.32$, V_S^* decreases faster to a zero-value than the corresponding contact line velocities (figure 22*d*). The dominant lateral expansion, which converts the ascending 'semilunar' central sheet into a nearly rectangular one (discussed in § 3.2.2), is the primary reason for this rapid deceleration of the sheet. Figure 22 also depicts that the momentum of lamella interaction at $\tau = \tau_0$ is higher for lower Δx^* due to brief viscous dissipation before interaction. For $\Delta x^* = 2.25$, two lamellae interact at $\tau_0 \approx 0.68$ with a velocity $\approx 0.8V_0$, whereas for $\Delta x^* = 1.32$, the lamellae interact at $\tau_0 \approx 0.22$ with a much higher velocity $\approx 2.19V_0$.
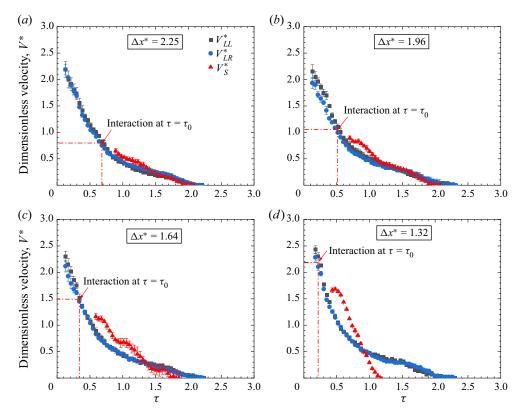
961 A17-32

Figure 22. (*a*–*d*) Temporal variation of the dimensionless contact line velocity of the left and right advancing lamellae (i.e. V_{LL}^* and V_{LR}^*, respectively) and the dimensionless velocity of the central uprising sheet (V_S^*), for different dimensionless inter-droplet spacings ($\Delta x^* = \Delta x/D_0$). All these velocities have been defined in figure 11. Here, τ_0 is the dimensionless time when the two lamellae start to interact. The Weber number was constant at 62 ± 1. Error bars represent the standard deviation around the mean.

Appendix B. Sensitivity analysis for estimating droplet-jet ratio ε

Figure 23 presents the image analysis procedure for estimating droplet jet ratio $\varepsilon (= d/w)$ and the sensitivity analysis of the image processing parameters. The image analysis algorithm (figure 23*a* i–iv) binarises an image of interest using a threshold value (within 0–255) determined by applying Otsu's method to the image using the MATLAB image processing toolbox. The binary image is then passed through a morphological erosion and dilation process using the same disk-shaped structuring element to remove the jet of interest from the central sheet. The boundary of the eroded and dilated binary image is then used as the separation line for the jet of interest. Therefore, an inappropriate radius of the disk element can lead to an underestimation of the jet length l_j, and thus can affect the estimation of the jet width w, which we estimated according to Sallam & Faeth (2003) as $w = A_j/l_j$.

In figure 23(*b*), we present the effect of the disk radius (in pixels) on estimating l_j for three typical peripheral jets in our experiments, namely jet 1, jet 2 and jet 3 (figure 23*a*-v), which have distinctly different lengths. For all cases, we find a minimum disk radius that allows avoiding an inappropriate separation line that truncates the actual jet and leads to the underestimation of l_j (see the left inset images of figure 23*b*). A disk radius greater or equal to the minimum disk radius fixes the separation line appropriately (see right inset images of figure 23*b*), and l_j becomes invariant by the disk radius, as observed
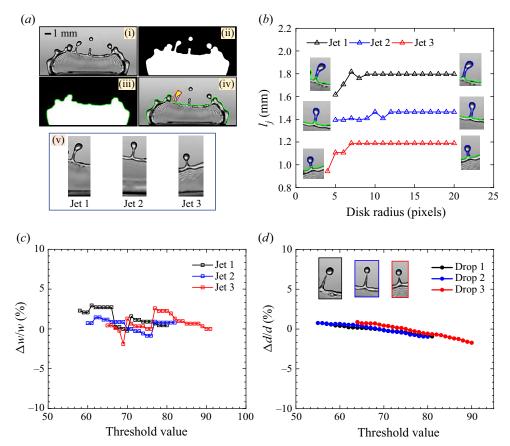
Figure 23. Sensitivity analysis of image processing parameters for estimating droplet-jet ratio $\varepsilon\,(= d/w)$. Here, d is the diameter of a secondary droplet detached from a jet of width w. (*a*) (i–iv) Image processing procedure to separate a peripheral jet of interest from the central sheet. A binary image in panel (*a*-ii) is achieved using a threshold value determined by applying Otsu's method (Otsu 1979) to the image in panel (*a*-i). Panel (*a*-iii) is achieved by eroding and dilating the binary image using the same disk-shaped structuring element for both operations. Subtracting panel (*a*-iii) from panel (*a*-ii) leads to separating the jet of interest by a green boundary from the central sheet and bounded by a red rectangle in panel (*a*-iv). Also, three different jets of interest (jet 1, jet 2 and jet 3) that are evaluated in panels (*b*,*c*) are shown in panel (*a*-v). For visual convenience, only the jet portion (cropped) of the actual processed images is presented in panel (*a*-v). (*b*) Effect of the radius of the morphological disk on the jet length l_j of the jets labelled in panel (*a*). For each case, the left inset images show examples of underestimated l_j scenario while the right ones show appropriately estimated l_j scenario. (*c*) Variation of the jet width difference $\Delta w/w$ as a function of the threshold level. Here, w is the jet width at Otsu's threshold level and $\Delta w = w - w_T$, with w_T as the jet width at any threshold level of consideration. (*d*) Variation of the secondary drop diameter difference $\Delta d/d$ as a function of the threshold level. Here, d is the drop diameter at Otsu's threshold level and $\Delta d = d - d_T$, with d_T as the drop diameter at any threshold level of consideration. The inset images show detached secondary droplets corresponding to their original jets shown in panel (*a*) and are bordered with the corresponding symbol colour.

in figure 23(*b*). To eliminate the disk radius sensitivity, we separate the jets of interest from their corresponding central sheets using a disk radius 2 pixels larger than the corresponding minimum disk radius. Therefore, estimating jet width w depends on the threshold value applied for binarisation.

Our measured w value for each jet of interest corresponds to the threshold value achieved by applying Otsu's method independently on each image. On a scale of pixel values of 0 to 255, the obtained Otsu's threshold values are 69, 71 and 76 respectively for the

images of jet 1, jet 2 and jet 3. We check the threshold sensitivity of w within $\pm 15\%$ of the Otsu's threshold value for each jet. Figure 23(c) shows the variation of the relative difference in jet width $\Delta w/w$ as a function of the threshold value, where $\Delta w = w - w_T$ with w_T representing the jet width at any value within $\pm 15\%$ of Otsu's threshold value. The maximum uncertainty observed is within $\pm 3\%$ of the measured values. It is noted that other jets observed in our experiments are within the range of lengths of these three typical jets. Also, for each jet of figure 23(c), the disk radius needed to separate the jet from the central sheet appropriately is found to be fixed for the considered threshold value range.

The measurement of the secondary droplet diameter d depends only on the threshold value. The variation of the relative difference in secondary droplet diameter, i.e. $\Delta d/d$, is shown as a function of threshold value in figure 23(d). Here, $\Delta d = d - d_T$, where d_T is the drop diameter at any threshold value within $\pm 15\%$ of Otsu's threshold value. We find that the maximum uncertainty in drop diameter measurement is within $\pm 2\%$ of the measured values. It is noted that d is measured as a mean diameter from ten consecutive images of the secondary droplet's trajectory, and accordingly, for each threshold value, d_T is also evaluated as a mean diameter from ten consecutive images. In summary, combining the uncertainties of d and w measurements, we estimate that, depending on the image processing parameters, the uncertainty of droplet-jet ratio (ε) is less than $\pm 4\%$ of the estimated value.

REFERENCES

AGBAGLAH, G. & DEEGAN, R.D. 2014 Growth and instability of the liquid rim in the crown splash regime. *J. Fluid Mech.* **752**, 485–496.

AGBAGLAH, G., JOSSERAND, C. & ZALESKI, S. 2013 Longitudinal instability of a liquid rim. *Phys. Fluids* **25** (2), 022103.

ARTMAN-BREITUNG, M., WATSON, D.A. & DICKERSON, A.K. 2021 Simultaneous impact of twin drops on a semi-infinite liquid target. *Phys. Fluids* **33** (10), 102110.

BARNES, H.A., HARDALUPAS, Y., TAYLOR, A.M.K.P. & WILKINS, J.H. 1999 An investigation of the interaction between two adjacent impinging droplets. In *Proceedings of the 15th International Conference on Liquid Atomisation and Spray Systems (ILASS), Toulouse, France* (ed. G. Lavergne), pp. 1–7. ONERA.

BATZDORF, S., BREITENBACH, J., SCHLAWITSCHEK, C., ROISMAN, I.V., TROPEA, C., STEPHAN, P. & GAMBARYAN-ROISMAN, T. 2017 Heat transfer during simultaneous impact of two drops onto a hot solid substrate. *Intl J. Heat Mass Transfer* **113**, 898–907.

BENNETT, T. & POULIKAKOS, D. 1993 Splat-quench solidification: estimating the maximum spreading of a droplet impacting a solid surface. *J. Mater. Sci.* **28** (4), 963–970.

BREITENBACH, J., ROISMAN, I.V. & TROPEA, C. 2018 From drop impact physics to spray cooling models: a critical review. *Exp. Fluids* **59**, 55.

BREMOND, N., CLANET, C. & VILLERMAUX, E. 2007 Atomization of undulating liquid sheets. *J. Fluid Mech.* **585**, 421–456.

BURZYNSKI, D.A., ROISMAN, I.V. & BANSMER, S.E. 2020 On the splashing of high-speed drops impacting a dry surface. *J. Fluid Mech.* **892**, A2.

CHEN, C.-K., CHEN, S.-Q., YAN, W.-M., LI, W.-K. & LIN, T.-H. 2020 Experimental study on two water drops successively impinging on a solid surface. *AIP Adv.* **10** (8), 085006.

COSSALI, G.E., COGHE, A.L.D.O. & MARENGO, M. 1997 The impact of a single drop on a wetted solid surface. *Exp. Fluids* **22** (6), 463–472.

COSSALI, G., MARENGO, M. & SANTINI, M. 2004 Impact of single and multiple drop array on a liquid film. In *19th Annual Meeting of ILASS, Nottingham, UK, 06-08/09/2004*, pp. 1–8. ILASS Europe.

COSSALI, G.E., MARENGO, M. & SANTINI, M. 2007 Splashing characteristics of multiple and single drop impacts onto a thin liquid film. In *Proceedings of the 6th International Conference on Multiphase Flow, Leipzig, Germany* (ed. Martin Sommerfeld). ICMF.

DEENDARLIANTO, TAKATA, Y., KOHNO, M., HIDAKA, S., WAKUI, T., MAJID, A.I., KUNTORO, H.Y., INDARTO & WIDYAPARAGA, A. 2016 The effects of the surface roughness on the dynamic behavior of the successive micrometric droplets impacting onto inclined hot surfaces. *Intl J. Heat Mass Transfer* **101**, 1217–1226.

EGGERS, J., FONTELOS, M.A., JOSSERAND, C. & ZALESKI, S. 2010 Drop dynamics after impact on a solid wall: theory and simulations. *Phys. Fluids* **22** (6), 062101.

ERSOY, N.E. & ESLAMIAN, M. 2020 Central uprising sheet in simultaneous and near-simultaneous impact of two high kinetic energy droplets onto dry surface and thin liquid film. *Phys. Fluids* **32** (1), 012108.

FAßMANN, B.W., BANSMER, S.E., MÖLLER, T.J., RADESPIEL, R. & HARTMANN, M. 2013 High velocity impingement of single droplets on a dry smooth surface. *Exp. Fluids* **54**, 1516.

FEST-SANTINI, S., STEIGERWALD, J., SANTINI, M., COSSALI, G.E. & WEIGAND, B. 2021 Multiple drops impact onto a liquid film: direct numerical simulation and experimental validation. *Comput. Fluids* **214**, 104761.

FUJIMOTO, H., ITO, S. & TAKEZAKI, I. 2002 Experimental study of successive collision of two water droplets with a solid. *Exp. Fluids* **33** (3), 500–502.

FUJIMOTO, H., OGINO, T., HATTA, N. & TAKUDA, H. 2001 Numerical simulation of successive collision of two liquid droplets with a solid wall. *ISIJ Intl* **41** (5), 454–459.

FUJIMOTO, H., TONG, A.Y. & TAKUDA, H. 2008 Interaction phenomena of two water droplets successively impacting onto a solid surface. *Intl J. Therm. Sci.* **47** (3), 229–236.

GILET, T. & BOUROUIBA, L. 2015 Fluid fragmentation shapes rain-induced foliar disease transmission. *J. R. Soc. Interface* **12** (104), 20141092.

GORDILLO, J.M. & GEKLE, S. 2010 Generation and breakup of worthington jets after cavity collapse. Part 2. Tip breakup of stretched jets. *J. Fluid Mech.* **663**, 331–346.

GORDILLO, J.M., RIBOUX, G. & QUINTERO, E.S. 2019 A theory on the spreading of impacting droplets. *J. Fluid Mech.* **866**, 298–315.

GORIN, B., DI MAURO, G., BONN, D. & KELLAY, H. 2022 Universal aspects of droplet spreading dynamics in newtonian and non-Newtonian fluids. *Langmuir* **38** (8), 2608–2613.

GUGGILLA, G., NARAYANASWAMY, R. & PATTAMATTA, A. 2020 An experimental investigation into the spread and heat transfer dynamics of a train of two concentric impinging droplets over a heated surface. *Expl Therm. Fluid Sci.* **110**, 109916.

GULTEKIN, A., ERKAN, N., OZDEMIR, E., COLAK, U. & SUZUKI, S. 2021 Simultaneous multiple droplet impact and their interactions on a heated surface. *Expl Therm. Fluid Sci.* **120**, 110255.

HOEPFFNER, J. & PARÉ, G. 2013 Recoil of a liquid filament: escape from pinch-off through creation of a vortex ring. *J. Fluid Mech.* **734**, 183–197.

JOSSERAND, C. & THORODDSEN, S.T. 2016 Drop impact on a solid surface. *Annu. Rev. Fluid Mech.* **48** (1), 365–391.

KRECHETNIKOV, R. 2010 Stability of liquid sheet edges. *Phys. Fluids* **22** (9), 092101.

LEJEUNE, S. & GILET, T. 2019 Drop impact close to the edge of an inclined substrate: liquid sheet formation and breakup. *Phys. Rev. Fluids* **4** (5), 053601.

LEJEUNE, S., GILET, T. & BOUROUIBA, L. 2018 Edge effect: liquid sheet and droplets formed by drop impact close to an edge. *Phys. Rev. Fluids* **3** (8), 083601.

LIANG, G. & MUDAWAR, I. 2016 Review of mass and momentum interactions during drop impact on a liquid film. *Intl J. Heat Mass Transfer* **101**, 577–599.

LIANG, G., YU, H., CHEN, L. & SHEN, S. 2020 Interfacial phenomena in impact of droplet array on solid wall. *Acta Mech.* **231** (1), 305–319.

LIANG, G., ZHANG, T., YU, H., CHEN, H. & SHEN, S. 2018 Simultaneous impact of multiple droplets on liquid film. *J. Ind. Engng Chem.* **65**, 51–61.

LIU, H.-C., KIJANKA, P. & URBAN, M.W. 2020 Fluid surface tension evaluation using capillary wave measurement with optical coherence tomography. *AIP Adv.* **10** (5), 055121.

LUO, J., WU, S.-Y., XIAO, L. & CHEN, Z.-L. 2021 Hydrodynamics and heat transfer of multiple droplets successively impacting on cylindrical surface. *Intl J. Heat Mass Transfer* **180**, 121749.

MARENGO, M., ANTONINI, C., ROISMAN, I.V. & TROPEA, C. 2011 Drop collisions with simple and complex surfaces. *Curr. Opin. Colloid Interface Sci.* **16** (4), 292–302.

MOORE, M.R., WHITELEY, J.P. & OLIVER, J.M. 2018 On the deflection of a liquid jet by an air-cushioning layer. *J. Fluid Mech.* **846**, 711–751.

MOREIRA, A.L.N., MOITA, A.S. & PANAO, M.R. 2010 Advances and challenges in explaining fuel spray impingement: how much of single droplet impact research is useful? *Prog. Energy Combust. Sci.* **36** (5), 554–580.

OTSU, N. 1979 A threshold selection method from gray-level histograms. *IEEE Trans. Syst. Man Cybern.* **9** (1), 62–66.

PETERS, I.R., VAN DER MEER, D. & GORDILLO, J.M. 2013 Splash wave and crown breakup after disc impact on a liquid surface. *J. Fluid Mech.* **724**, 553–580.

RAMAN, K.A., JAIMAN, R.K., LEE, T.-S. & LOW, H.-T. 2016 Lattice Boltzmann study on the dynamics of successive droplets impact on a solid surface. *Chem. Engng Sci.* **145**, 181–195.

RAYLEIGH, LORD 1878 On the instability of jets. *Proc. Lond. Math. Soc.* **1** (1), 4–13.

RIBOUX, G. & GORDILLO, J.M. 2015 The diameters and velocities of the droplets ejected after splashing. *J. Fluid Mech.* **772**, 630–648.

ROISMAN, I.V. 2010 On the instability of a free viscous rim. *J. Fluid Mech.* **661**, 206–228.

ROISMAN, I.V., BERBEROVIĆ, E. & TROPEA, C. 2009 Inertia dominated drop collisions. I. On the universal flow in the lamella. *Phys. Fluids* **21** (5), 052103.

ROISMAN, I.V., HORVAT, K. & TROPEA, C. 2006 Spray impact: rim transverse instability initiating fingering and splash, and description of a secondary spray. *Phys. Fluids* **18** (10), 102104.

ROISMAN, I.V., LEMBACH, A. & TROPEA, C. 2015 Drop splashing induced by target roughness and porosity: the size plays no role. *Adv. Colloid Interface Sci.* **222**, 615–621.

ROISMAN, I.V., PRUNET-FOCH, B., TROPEA, C. & VIGNES-ADLER, M. 2002 Multiple drop impact onto a dry solid substrate. *J. Colloid Interface Sci.* **256** (2), 396–410.

ROZHKOV, A., PRUNET-FOCH, B. & VIGNES-ADLER, M. 2002 Impact of water drops on small targets. *Phys. Fluids* **14** (10), 3485–3501.

ROZHKOV, A., PRUNET-FOCH, B. & VIGNES-ADLER, M. 2004 Dynamics of a liquid lamella resulting from the impact of a water drop on a small target. *Proc. R. Soc. Lond.* A **460** (2049), 2681–2704.

SALLAM, K.A. & FAETH, G.M. 2003 Surface properties during primary breakup of turbulent liquid jets in still air. *AIAA J.* **41** (8), 1514–1524.

SCHULKES, R.M.S.M. 1996 The contraction of liquid filaments. *J. Fluid Mech.* **309**, 277–300.

TAYLOR, G.I. 1950 The instability of liquid surfaces when accelerated in a direction perpendicular to their planes. I. *Proc. R. Soc. Lond.* A **201** (1065), 192–196.

THORODDSEN, S.T., ETOH, T.G. & TAKEHARA, K. 2008 High-speed imaging of drops and bubbles. *Annu. Rev. Fluid Mech.* **40**, 257–285.

THORODDSEN, S.T., TAKEHARA, K. & ETOH, T.G. 2012 Micro-splashing by drop impacts. *J. Fluid Mech.* **706**, 560–570.

TONG, A.Y., KASLIWAL, S. & FUJIMOTO, H. 2007 On the successive impingement of droplets onto a substrate. *Numer. Heat Transf.* A **52** (6), 531–548.

UKIWE, C. & KWOK, D.Y. 2005 On the maximum spreading diameter of impacting droplets on well-prepared solid surfaces. *Langmuir* **21** (2), 666–673.

UKIWE, C., MANSOURI, A. & KWOK, D.Y. 2005 The dynamics of impacting water droplets on alkanethiol self-assembled monolayers with co-adsorbed CH_3 and CO_2H terminal groups. *J. Colloid Interface Sci.* **285** (2), 760–768.

VERNAY, C., RAMOS, L. & LIGOURE, C. 2015 Free radially expanding liquid sheet in air: time-and space-resolved measurement of the thickness field. *J. Fluid Mech.* **764**, 428–444.

VILLERMAUX, E. & BOSSA, B. 2011 Drop fragmentation on impact. *J. Fluid Mech.* **668**, 412–435.

VILLERMAUX, E. & CLANET, C. 2002 Life of a flapping liquid sheet. *J. Fluid Mech.* **462**, 341–363.

WANG, Y. & BOUROUIBA, L. 2018 Non-isolated drop impact on surfaces. *J. Fluid Mech.* **835**, 24–44.

WANG, Y. & BOUROUIBA, L. 2021 Growth and breakup of ligaments in unsteady fragmentation. *J. Fluid Mech.* **910**, A39.

WANG, Y., DANDEKAR, R., BUSTOS, N., POULAIN, S. & BOUROUIBA, L. 2018 Universal rim thickness in unsteady sheet fragmentation. *Phys. Rev. Lett.* **120** (20), 204503.

WIBOWO, T., WIDYATAMA, A., KAMAL, S., INDARTO & DEENDARLIANTO 2021 The effect of ethylene glycol concentration on the interfacial dynamics of the successive droplets impacting onto a horizontal hot solid surface. *Intl J. Therm. Sci.* **159**, 106594.

WORTHINGTON, A.M. 1877 On the forms assumed by drops of liquids falling vertically on a horizontal plate. *Proc. R. Soc. Lond.* **25** (171–178), 261–272.

YARIN, A.L., *et al.* 2006 Drop impact dynamics: splashing, spreading, receding, bouncing. *Annu. Rev. Fluid Mech.* **38** (1), 159–192.

YARIN, A.L., ROISMAN, I.V. & TROPEA, C. 2017 *Collision Phenomena in Liquids and Solids*. Cambridge University Press.

YARIN, A.L. & WEISS, D.A. 1995 Impact of drops on solid surfaces: self-similar capillary waves, and splashing as a new type of kinematic discontinuity. *J. Fluid Mech.* **283**, 141–173.

ZHANG, L.V., BRUNET, P., EGGERS, J. & DEEGAN, R.D. 2010 Wavelength selection in the crown splash. *Phys. Fluids* **22** (12), 122105.

ZHANG, H., GAO, Y., ZHANG, X., YI, X., DU, Y., HE, F., JIN, Z. & HAO, P. 2021 Characteristics of secondary droplets produced by the impact of drops onto a smooth surface. *Adv. Aerodyn.* **3**, 35.

ZHANG, B., LI, J., GUO, P. & LV, Q. 2017 Experimental studies on the effect of Reynolds and Weber numbers on the impact forces of low-speed droplets colliding with a solid surface. *Exp. Fluids* **58**, 125.